Chapter-6

Results and Discussion

6.1 Introduction

The use of elastic, elastic-plastic, visco-plastic solutions under various kinds of loads are now widespread in fracture mechanics area. Applications of such analyses are necessary for the interpretation of the local/ global effects in crack problems under complex practical engineering environment. The primary concern is to predict, as accurately as possible, the life of structures in critical applications. In this respect, various fracture characterizing parameters are now in common use in identifying the critical conditions of crack tip fields under various types of loads. With this view in mind, the constitutive equations for plastically compressible rate dependent elastic visco-plastic solids with hardening-hardening and hardening-softening-hardening flow rules have been considered in the chapter 4 and now it seems natural to investigate and verify the behavior of these constitutive equations under different loading conditions.

In the subsequent sections, the details of boundary conditions, loadings etc along with numerical results are described. All the numerical analyses have been carried out under the assumption of small scale yielding and plane strain deformation conditions. Initially analyses are performed under monotonic loads and then the results under cyclic loadings are presented. In the elastic-viscoplastic analyses, the role of hydrostatic stress in the yield criterion has been assumed and also both associated and non-associated flow rules are used. Several material models have been used to reflect the behavior of the present plastically compressible elastic viscoplastic response.

6.2 Problem Definition with Boundary Conditions

Here, plain strain calculations are carried out for a semi circular region of radius R_0=2.0 in arbitrary units as shown in Fig.5.3a. The loading and the geometry are symmetric with respect to the crack plane. There is a notch of initial radius b_0 =0.001 in the same arbitrary units with its centre at the origin of the coordinate system as shown in figure 5.3b, so that $R_0/b_0 = 2\,x\,10^3$.

6.2.1 Boundary Conditions for Monotonic Loading

It is well known that if a solid is loaded to a sufficiently low stress level a theoretical investigation can be undertaken much more readily than if the size of yield zone is unrestricted. This is because linear elastic stress-intensity factors can be used to give the surrounding elastic field, and it is possible to employ a boundary layer formulation to determine the elastic-plastic field in the immediate vicinity of the crack tip. Here, the actual elastic-plastic problem is replaced by a problem formulated in boundary layer style, whereby a semi infinite crack in an infinite body is considered and the actual conditions of boundary loading are replaced by the asymptotic boundary conditions.

Here, in the current analysis it is true that it is difficult to imagine a situation where ssy conditions will prevail at the crack tip in the present material and equation (2.1) is inaccurate within and near a small crack tip yield zone. In the equation the other non-singular terms have been omitted in the present analysis. Present geometry and loading conditions have been provided in order to formulate the problem in boundary layer style, whereby a semi infinite crack in an infinite body is considered and the actual conditions of boundary loading are replaced by the asymptotic boundary conditions through equations (6.1) and (6.2).

Plain strain mode I small scale yielding analyses are carried out with following displacement rate boundary conditions imposed on the outer semi-circular boundary.

$$\dot{u}_1 = \frac{2(1+\nu)\dot{K}_\mathrm{I}}{E}\sqrt{\frac{R}{2\pi}}\cos\left(\frac{\theta}{2}\right)\left[1-2\nu+\sin^2\left(\frac{\theta}{2}\right)\right] \qquad (6.1)$$

And

$$\dot{u}_2 = \frac{2(1+\nu)\dot{K}_\mathrm{I}}{E}\sqrt{\frac{R}{2\pi}}\sin\left(\frac{\theta}{2}\right)\left[2-2\nu+\cos^2\left(\frac{\theta}{2}\right)\right] \qquad (6.2)$$

Where

$$R = \sqrt{((y^1)^2+(y^2)^2)} \qquad \theta = \tan^{-1}\left(\frac{y^2}{y^1}\right) \qquad (6.3)$$

and K_I is the stress intensity factor. For small scale yielding, the corresponding value of the applied *J*, J_{app} is given by (Rice, 1968).

$$J_{\mathrm{app}} = K_\mathrm{I}^2\frac{(1-\nu^2)}{E} \qquad (6.4)$$

The K_I field displacement in equations (6.1) and (6.2) are imposed on the semi-circular boundary. Crack surfaces are assumed to be traction free and symmetry conditions are imposed on $y^2 = 0$. A constant value of $\dot{K_\mathrm{I}}/\sigma_0\dot{\varepsilon_0}\sqrt{b_0} = 31.62$ is prescribed and this normalized loading rate corresponds to $\dot{K}_\mathrm{I} = 1\ MPa\sqrt{m}s^{-1}$. A linear incremental update with time step of size 0.0002 has been used to calculate the deformation history.

6.2.2 Boundary Conditions for Cyclic Loading

The K_I-field displacements expressed in Eqs. (6.1) and (6.2) that correspond to the linear isotropic elastic mode I crack tip field are imposed on the outer semi-circular boundary. The displacements at the boundary would be cycled corresponding to $(K_\mathrm{I})_{\mathrm{max}}$ and $(K_\mathrm{I})_{\mathrm{min}}$, similar to monotonic loading. A constant value $\dot{K_\mathrm{I}}/\sigma_0\dot{\varepsilon_0}\sqrt{b_0}$ = 31.62 is prescribed. This normalized

loading rate corresponds to $\dot{K}_{\mathrm{I}} = 1\ MPa\sqrt{m}s^{-1}$. In order to carry out the simulation under cyclic loading, several different constant amplitude loadings are applied to the model. Also a few cases of overloading have been considered. In addition to the different constant amplitude loading with load ratio, R = 0, R values of 0.33, 0.5 have also been considered for study. For all load cycles a triangular shape waveform is used. Simulated load cases are consisted of up to ten cycles:

(I) $(K_{\mathrm{I}})_{\max}/K_{\mathrm{ref}} = 0.5, \quad (K_{\mathrm{I}})_{\min} = 0$

(II) $(K_{\mathrm{I}})_{\max}/K_{\mathrm{ref}} = 1.0, \quad (K_{\mathrm{I}})_{\min} = 0$

(III) $(K_{\mathrm{I}})_{\max}/K_{\mathrm{ref}} = 1.5, \quad (K_{\mathrm{I}})_{\min}/K_{\mathrm{ref}} = 0.5$

(IV) $(K_{\mathrm{I}})_{\max}/K_{\mathrm{ref}} = 2.0, \quad (K_{\mathrm{I}})_{\min} = 0$

(V) $(K_{\mathrm{I}})_{\max}/K_{\mathrm{ref}} = 2.0, \quad (K_{\mathrm{I}})_{\min}/K_{\mathrm{ref}} = 1$

(VI) $(K_{\mathrm{I}})_{\max}/K_{\mathrm{ref}} = 1.0 \quad (K_{\mathrm{I}})_{\min} = 0$ with an overload $(K_{\mathrm{I}})_{\mathrm{overload}} = 1.5(K_{\mathrm{I}})_{\max}$ at fifth cycle

Where the reference stress intensity factor, K_{ref} is taken to be $\sigma_0\sqrt{1000b_0}$.

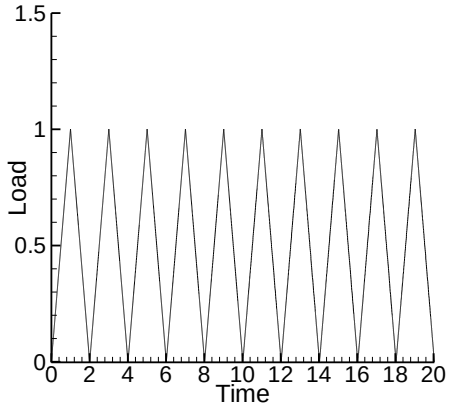

Figure 6.1: Cyclic loading used in present fatigue crack simulation

6.3 Convergence Studies

In order to test the accuracy of finite element results, comparison needs to be made with exact analytical solutions, if available. Alternatively, as the finite element method minimizes a prescribed functional then the solution will converge to the true value with increasing mesh density, Zienkiewicz (1979). Therefore, comparison of global response by mesh refinement technique is also an accepted procedure for such convergence studies. A part of the undeformed geometry with typical mesh pattern near to the crack tip has been shown in Fig. 6.1A.

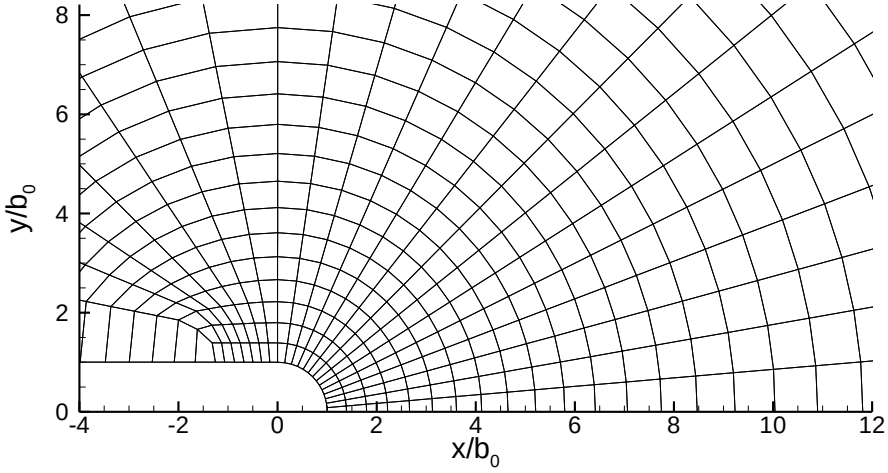

Figure 6.1A: Typical mesh used in the finite element simulation (near tip mesh)

6. 3.1 Mesh Convergence

In fracture mechanics, for the global response convergence with respect to mesh size, the two areas of interest are the crack tip region and the load application region. Therefore, applying the present visco-plasticity model on the semicircular geometry for the material mentioned in chapter 5, mesh convergence studies based on incremental plasticity theory have been

performed without using any special crack tip elements. In order to test the adequacy of the finite element mesh used, calculations were carried out with meshes consisting of 22 x 54, 22 x 64, and 22 x 74 quadrilateral elements. Figure 6.2 illustrates the curves of J_{app} given by Eq. (6.4) versus crack opening $(b/b_0 - 1)$ where b is the current crack opening at $y^1 = -0.004$ for material B. The values of J_{app} were within 2% over the range computed. Also contours of plastic strain were compared in the near tip region for material B and when it is plastically compressible ($\alpha_p = 0.28$), Fig. 6.3. It is reflected from the results that J_{app} versus CTOD results are quite stable for all the 3 cases however, the plastic strain contours reveal that the results from the 22 x 64 and 22 x 74 are in good agreement as compared to 22 x 54. Solutions were also obtained for other meshes and it was observed that except in the initial levels, the solutions were quite stable showing negligible differences at higher mesh densities. As a compromise between solution accuracy and computation time, the results to be presented were obtained using a 22 x 64 quadrilateral mesh.

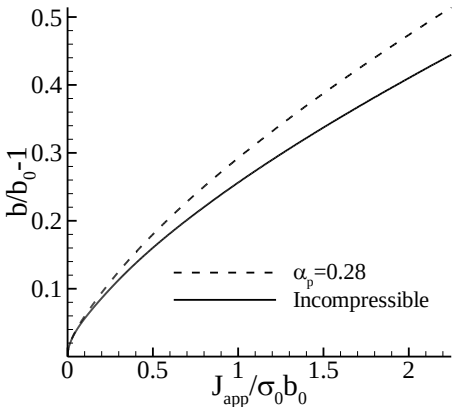

(a)

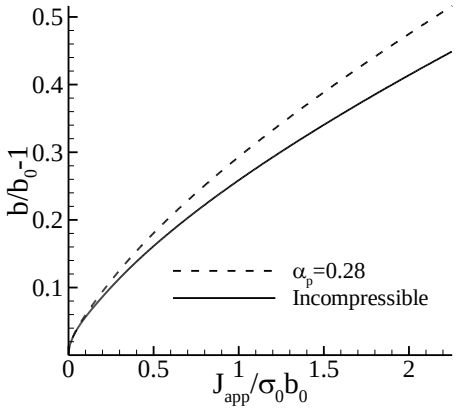

(b)

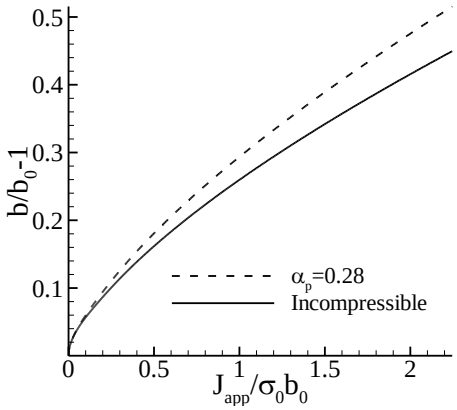

(c)

Figure 6.2: Crack-tip opening displacement $\delta_t(= b/b_0 - 1)$ versus applied *J*-integral, J_{app} in material B; a) 22 x 54 quadrilateral mesh, b) 22 x 64 quadrilateral mesh, c) 22 x 74 quadrilateral mesh

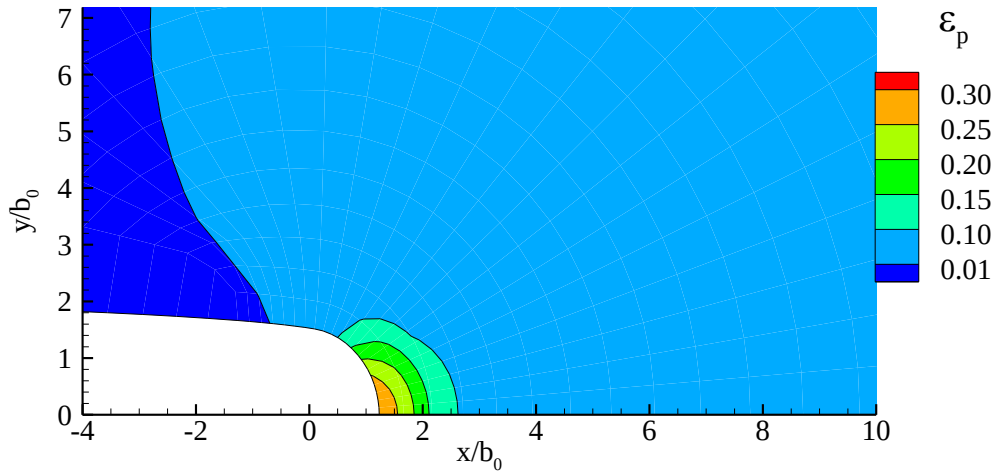

(a)

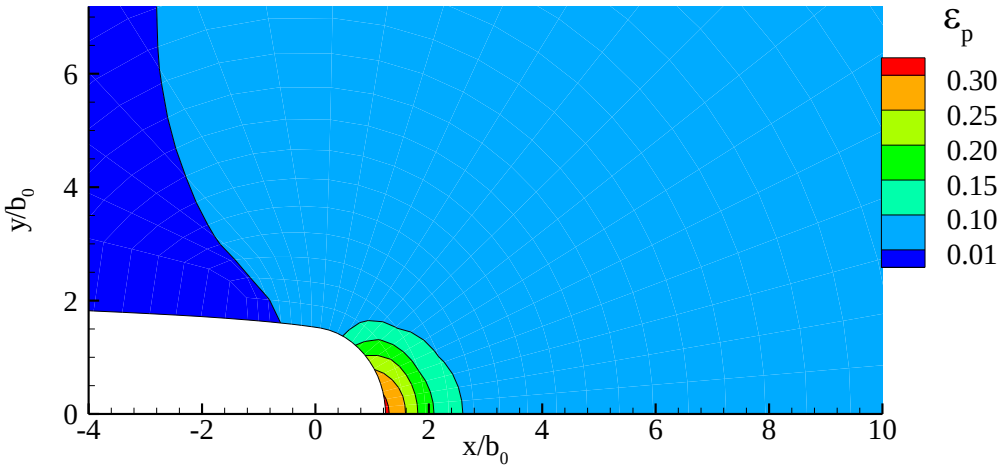

(b)

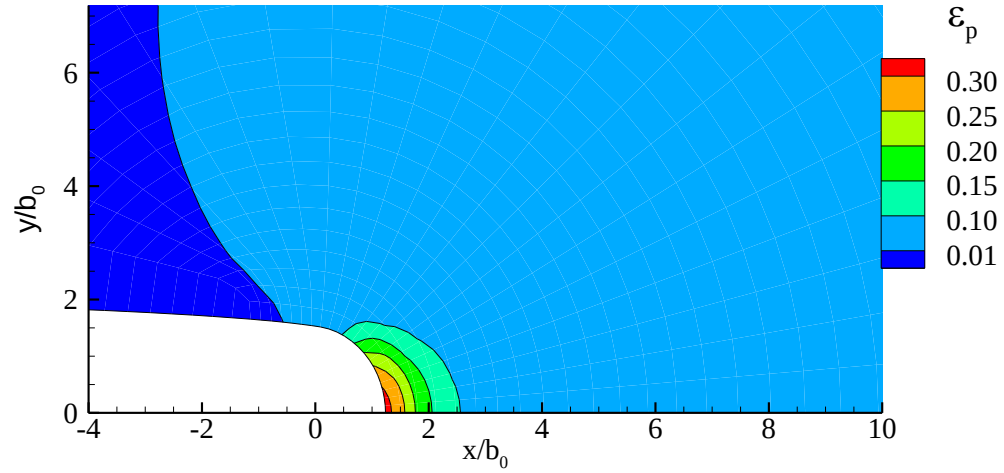

(c)

Figure 6.3: Plastic strain distribution for plastically compressible solid, material B, α_p = 0.28 , a) 22 x 54 quadrilateral mesh, b) 22 x 64 quadrilateral mesh, c) 22 x 74 quadrilateral mesh

6.3.2 Program Verification Analysis

The reliability of the present computational model has been further established by comparing the nature of the stress distributions in front of the crack tip. Fig. 6.4 presents the variations

of σ_{xx}, σ_{yy} and σ_{xy} with respect to x-coordinate distance from the crack tip (i.e. for $\theta = 0$) for the growing crack in material B and when it is plastically incompressible. The graph shows that very near to the crack tip the stress quantities are sensitive to the distance from the crack tip, however, after some distance these quantities become constant. The values of σ_{yy} are dominant near to the crack tip as expected. As a consequence, the result obtained in Fig. 6.4 has been considered sufficient to continue further investigations.

Due to the combined effects of various non-linear contributions in the present problem, the problem under scrutiny seems to be very complicated to be solved analytically. Also presently there is no experimental set up available to us for verification. Nonetheless, even though, the present results are not validated in a quantitative way with analytical solutions or qualitatively with experimental results, the results are validated with some earlier results in a qualitative way in number of places.

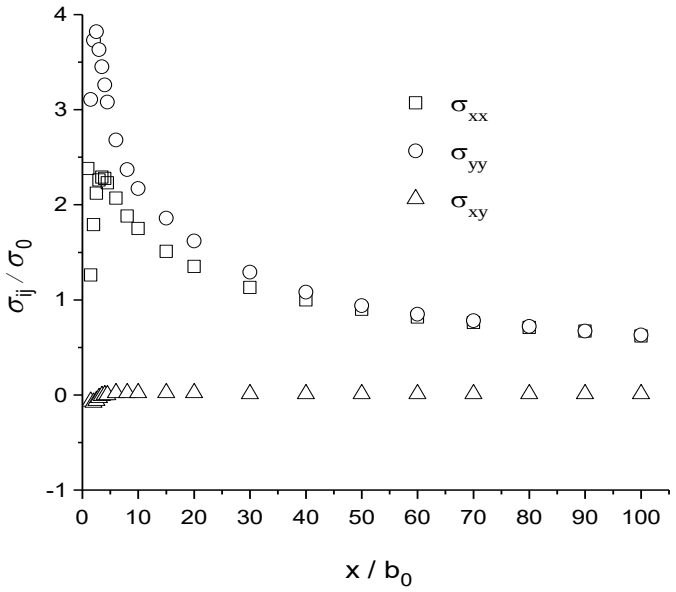

Figure 6.4: Stress distribution for a growing crack in material B, plastically incompressible, applied *J*-integral, $J_{app}/(\sigma_0 b_0) = 2.25$

6.4 Some Results under Monotonic Loading (Plastic Normality Condition)

Now some numerical results illustrating the performance of the constitutive equations described in chapter 4 and chapter 5 are presented for the semicircular plate geometry subjected to monotonic loading and when the constitutive equation is said to follow normality flow rule. These results are in no way meant to be conclusive for the purpose of proposing any fracture criteria.

6.4.1 Applied *J* versus Crack Tip Opening Displacement

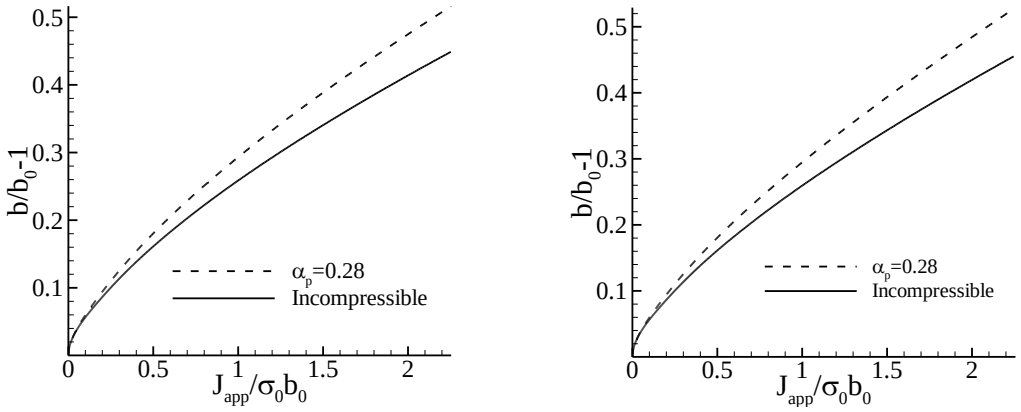

Figure 6.5: Curves of crack-tip opening displacement $(b/b_0 - 1)$ versus the applied J-integral, J_{app} for plastically incompressible and compressible hardening solid, a) Material B. b) Material C

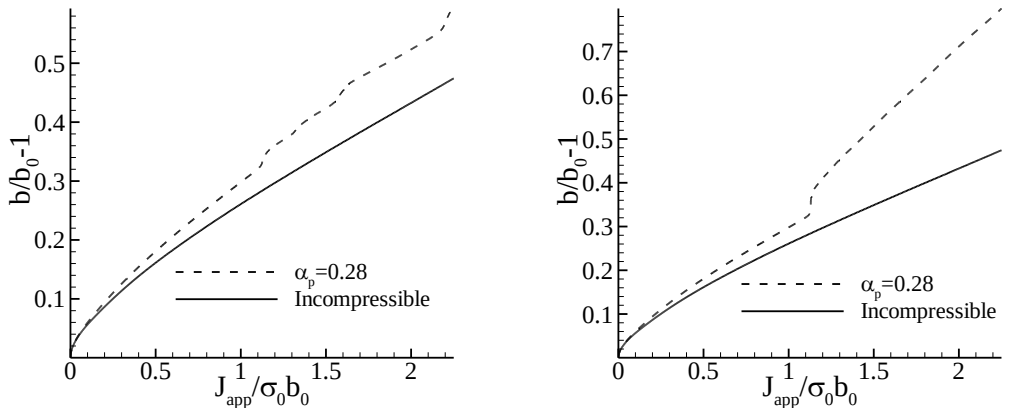

Figure 6.6: Curves of crack-tip opening displacement $(b/b_0 - 1)$ versus the applied J-integral, J_{app} for plastically incompressible and compressible solids. a) Material E. b) Material G

Figures 6.5 and 6.6 show the effects of hardening-hardening and hardening–softening–hardening type hardness function and plastic compressibility on the relation between J_{app} Eq. (6.4), and the crack tip opening displacement $(b/b_0 - 1)$ for the three hardening functions considered.

Results are shown in Figs.6.5 and 6.6 for both plastically incompressible and compressible $(\alpha_{\text{p}} = 0.28)$ solids. For materials E and G, where the variation of flow strength is of the hardening–softening–hardening type, there are more or less abrupt jumps in the curves. As will be shown subsequently, the more or less abrupt jumps in Fig.6.6 are associated with the evolution of a region of localized deformation that develops in front of the initial crack tip for materials E and G With, $(\alpha_{\text{p}} = 0.28)$ but not when these materials are incompressible. Thus, plastic compressibility influences the variation of crack opening with the J_{app}.

For small-scale yielding of power law strain hardening materials, the crack tip opening displacement is expected to be proportional to J_{app}, see e.g. Refs. (McMeeking, 1977; Rice, 1968; Shih, 1981) as a consequence of the emergence of a Hutchinson-Rice-Rosengren (HRR) field (Hutchinson, 1968; Rice and Rosengren, 1968). The constant of proportionality is strongly dependent on the strain hardening exponent *N* and more weakly dependent on the yield strain σ_0/E (increasing with increasing yield strain) (Shih, 1981). For example, with *N* = 0.1, the constant of proportionality is ≈ 0.5, while with *N* = 0.5, it is ≈ 0.2. Here, *N*=1 since linear hardening prevails in each segment, so that the small values of $(b/b_0 - 1)$ for a given value of J_{app} are consistent with linear hardening. It is also worth noting that the results in Figs.6.5 and 6.6 give an increasing value of the crack opening displacement $(b/b_0 - 1)$ for a given value of J_{app} with increasing plastic compressibility.

However, since the relation between $(b/b_0 - 1)$ and J_{app} in Figs. 6.5 and 6.6 is nonlinear, the results of (Shih, 1981) imply that a fully developed HRR does not prevail in the calculations here. One possibility is that we analyze a notch rather than a mathematically sharp crack, which together with finite deformation effects precludes the HRR field from emerging. Another possibility is that small scale yielding is lost because of the extent of the plastic zone. However, plots of effective plastic strain presented subsequently in Figs. 6.7 and 6.8 shows that plastic zone sizes remain small compared to R_0 (a maximum extent of about 0.02 R_0). Plotting the data in Figs. 6.5 and 6.6 on a log–log scale shows that in all cases $J \approx (b/b_0 - 1)^{1/2}$ for small values of $J/(\sigma_0 b_0)$. Subsequently, for larger values of $J/(\sigma_0 b_0)$, the slope of the log–log plot indicates a power law relation of the form $J \approx (b/b_0 - 1)^p$ with p generally in the range 0.70 to 0.85 for the largest values of $J/(\sigma_0 b_0)$ considered. This suggests that the sharp crack solution is being approached with increasing *J*.

6.4.2 Plastic Zone Shape and Size

The plastic zone shape and size at the crack tip is of fundamental importance in the fracture behavior of materials and informative for the path invariance character of contour integrals. This is also important for the prediction of the direction of crack propagation as well as the standardization of fracture mechanics test piece dimensions.

Figures 6.7 and 6.8 show distributions of plastic strain, $\varepsilon_{\mathrm{p}} = \int \dot{\varepsilon}_{\mathrm{p}}\, dt$, with $\dot{\varepsilon}_{\mathrm{p}}$ is given by Eq. (4.5). Here, and subsequently, we use the notation $x = y^1$ and $y = y^2$ and normalize distances by b_0. For the viscoplastic constitutive relation used in the calculations here, there is no sharp yield point and hence no well defined plastic zone. However, the contour values 0.001 or 0.002 indicate the extent of the region with any appreciable plastic straining and so a value in this range can be taken to indicate the plastic zone size and shape.

Figure 6.7 shows distributions for material B, which hardens monotonically, for a plastically incompressible solid, $\alpha_{\mathrm{p}} = 0.333333$, Fig.6.7a, and for a solid with $\alpha_{\mathrm{p}} = 0.28$, Fig.6.7b. With $\alpha_{\mathrm{p}} = 0.28$, the extent of the larger strain region $\varepsilon_{\mathrm{p}} > 0.01$ is increased and the shape of the contours has changed from the kidney-like shape for the plastically incompressible solid.

For a plastically incompressible solid,$\alpha_{\mathrm{p}} = 0.333333$, in Fig. 6.8a, where the material has a hardening–softening–hardening strength given by Eq. (4.6), the contours for $0.01 \geq \varepsilon_{\mathrm{p}}$ are nearly identical to those for the hardening solid in Fig.6.7a. Thus, the change in near tip response does not have a noticeable effect at the distances seen in Fig.6.8a. For the compressible solid in Fig.6.8b, $\alpha_{\mathrm{p}} = 0.28$, some difference can be seen. In particular, the 0.01 contour is tilted more ahead of the crack tip and is larger.

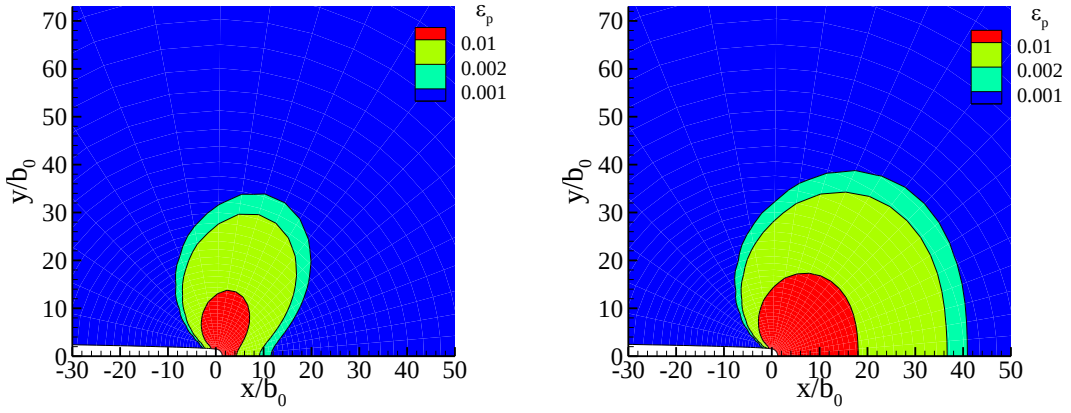

(a) (b)

Figure 6.7: Distribution of plastic strain, ε_{p}, for material B with $J_{\mathrm{app}}/(\sigma_0 b_0) = 2.25$ a) Plastically incompressible solid, $\alpha_{\mathrm{p}} = 0.333333$. b) Plastically compressible solid, $\alpha_{\mathrm{p}} = 0.28$

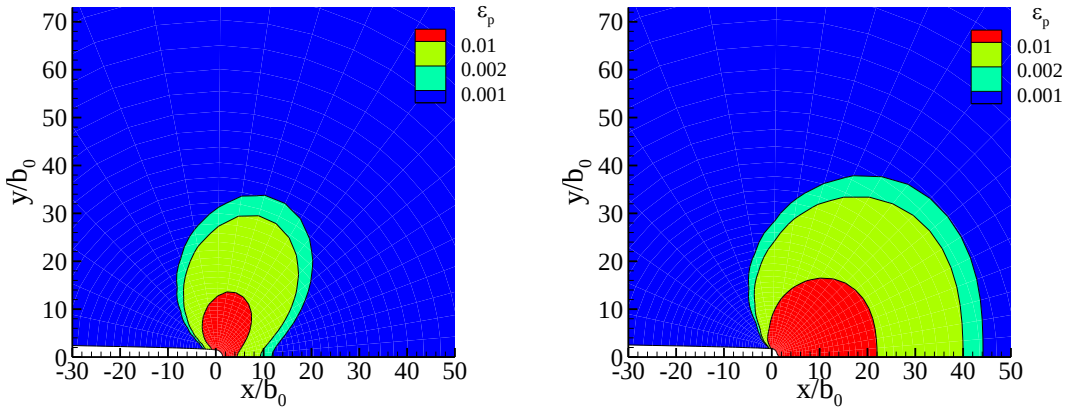

(a) (b)

Figure 6.8: Distribution of plastic strain, ε_{p}, for material G with $J_{\mathrm{app}}/(\sigma_0 b_0) = 2.25$ a) Plastically incompressible solid, $\alpha_{\mathrm{p}} = 0.333333$. b) Plastically compressible solid, $\alpha_{\mathrm{p}} = 0.28$

The main difference in the extent of plastic straining between the plastically incompressible and compressible solids in Figs.6.7 and 6.8 is along the x-axis, where the contours for $\alpha_{\mathrm{p}} =$

0.28 extend about a factor of 4 farther than for the corresponding plastically incompressible solid. On the other hand, the extent of these contours in the y-direction is rather insensitive to the plastic compressibility.

The differences in plastic strain distributions between the hardening and hardening–softening–hardening plastic strain distributions are small at the scale in Figs. 6.7 and 6.8. Thus, at least up to the largest value of J_{app}, considered in the calculations here, the extent of the zone with significant plastic straining is not very sensitive to whether the material is hardening or hardening–softening–hardening. However, as will be shown subsequently, the near crack tip fields are very sensitive to this. On the other hand, at the scale in Figs. 6.7 and 6.8, plastic compressibility has a significant effect on the plastic strain distributions.

In both Figs. 6.7 and 6.8, the extent of the $\varepsilon_{\mathrm{p}} = 0.001$ contour is confined to within distances of x/b_0 and y/b_0 less than 40 from the initial crack tip. This compares with the value of the ring radius of R_0/b_0 of $2\ x\ 10^3$ which indicates that the deviation from linearity in Figs. 6.7 and 6.8 is not a consequence of the loss of small scale yielding.

6.4.3 Near Crack Tip Fields

Now, attention is focused for studying the near crack tip fields of the materials under consideration. For comparison purposes, Fig. 6.9, shows contours of plastic strain, ε_{p}, and hydrostatic stress, $\sigma_{\mathrm{h}}/\sigma_0$, for material B, a hardening material. As expected, the maximum plastic strain occurs on the crack blunting crack surface and the maximum hydrostatic stress is on the symmetry plane away from the crack tip. Even though the distributions in Fig. 6.9 are for a plastically compressible solid, $\alpha_{\mathrm{p}} = 0.28$, the distributions of plastic strain and

hydrostatic stress differ little, at least qualitatively, from those for a plastically incompressible Mises material.

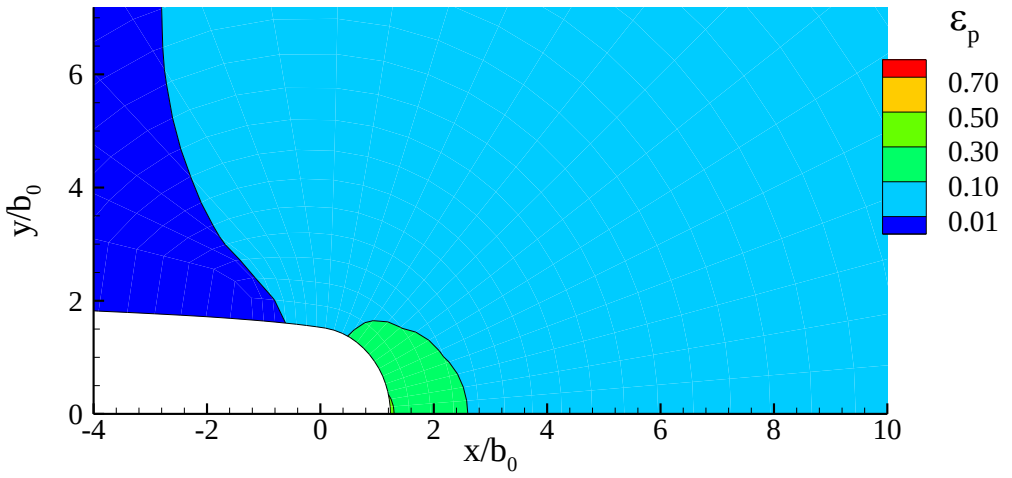

(a)

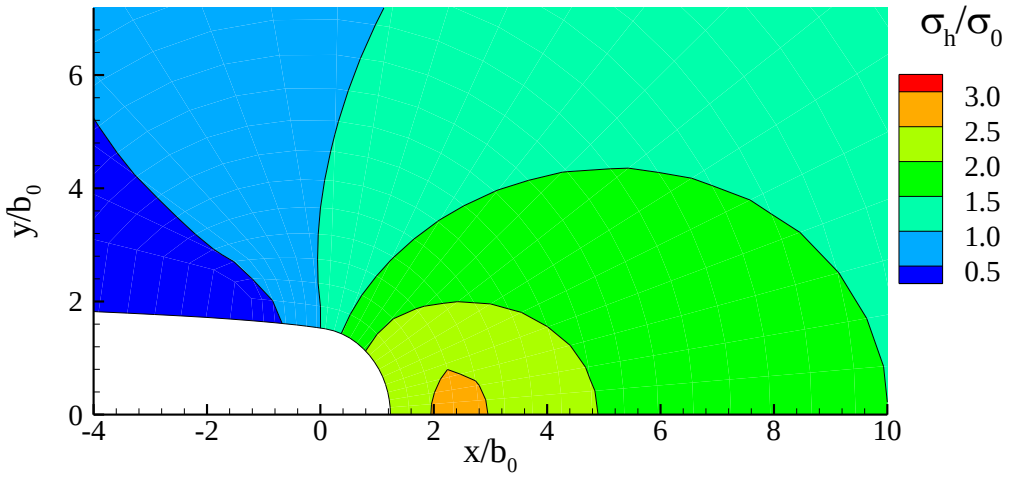

(b)

Figure 6.9: Field distributions in the crack tip vicinity for material B (a hardening material) with $\alpha_p = 0.28$ at $J_{app}/(\sigma_0 b_0) = 2.25$. a) Plastic strain, ε_p b) Hydrostatic stress, σ_h/σ_0

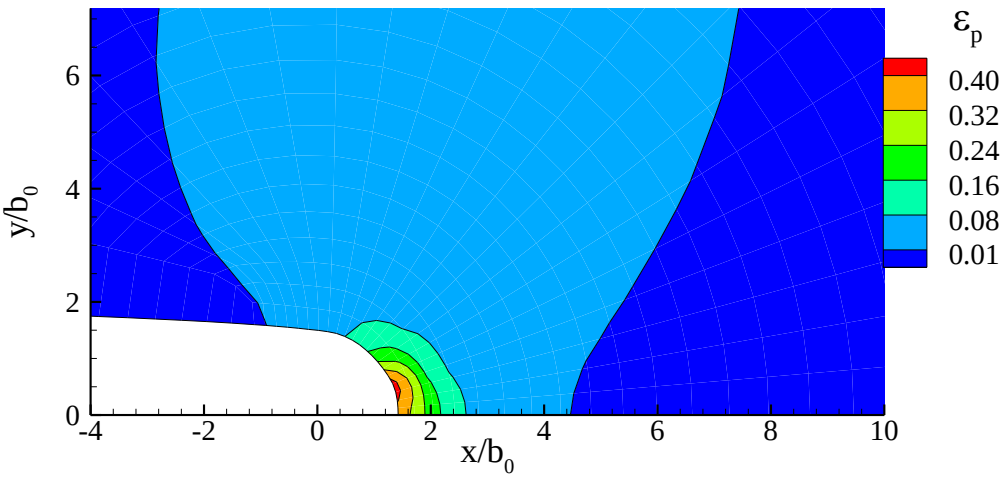
ε_p
0.40
0.32
0.24
0.16
0.08
0.01
y/b0
x/b0
0
2
4
6
-4
-2
0
2
4
6
8
10

(a)

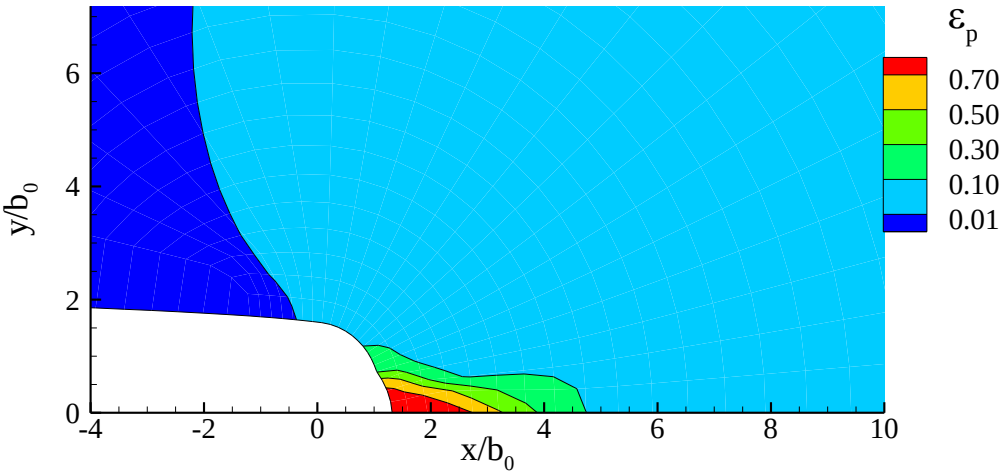
ε_p
0.70
0.50
0.30
0.10
0.01
y/b0
x/b0
0
2
4
6
-4
-2
0
2
4
6
8
10

(b)

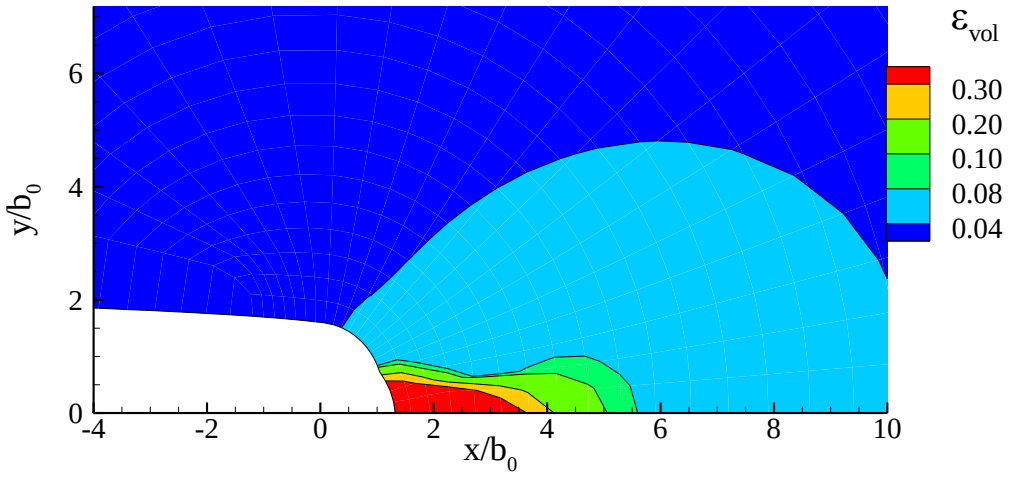

(c)

Figure 6.10: Strain distributions in the crack tip vicinity for material E at $J_{\text{app}}/(\sigma_0 b_0) = 2.25$. a) Distribution of ε_{p} for a plastically incompressible solid, $\alpha_{\text{p}} = 0.333333$. b) Distribution of ε_{p} for a plastically compressible solid, $\alpha_{\text{p}} = 0.28$. c) Distribution of ε_{vol} for a plastically compressible solid, $\alpha_{\text{p}} = 0.28$

Figures 6.10 – 6.12 show field distributions for material E which is a hardening- softening-hardening material with the transition from the softening branch to the subsequent hardening branch taking place at $\varepsilon_{\text{p}} = 0.6$. Unlike for the hardening material in Fig. 6.9, plastic compressibility has a major effect on the distributions.

In Fig. 6.10a, $\alpha_{\text{p}} = 0.333333$, there is a plastic strain concentration on the surface of the crack. On the other hand, with $\alpha_{\text{p}} = 0.28$, there is a region of intense plastic deformation emanating from the crack surface near the symmetry plane. This difference in deformation mode also leads to a difference in the shape of the deformed crack surface. Figure 6.10c shows the distribution of ε_{vol} for the plastically compressible solid, $= 0.28$, where

$$\varepsilon_{vol} = \int_0^t \mathrm{tr}(\boldsymbol{d})\, dt \qquad (6.5)$$

Since $\varepsilon_{\mathrm{vol}}$ is defined in terms of the total rate of deformation tensor it includes a small elastic contribution from $\boldsymbol{d}^e$. There is a rather large region where there are substantial volume changes ≥ 0.04 and the largest volume changes occur directly in front of the crack tip.

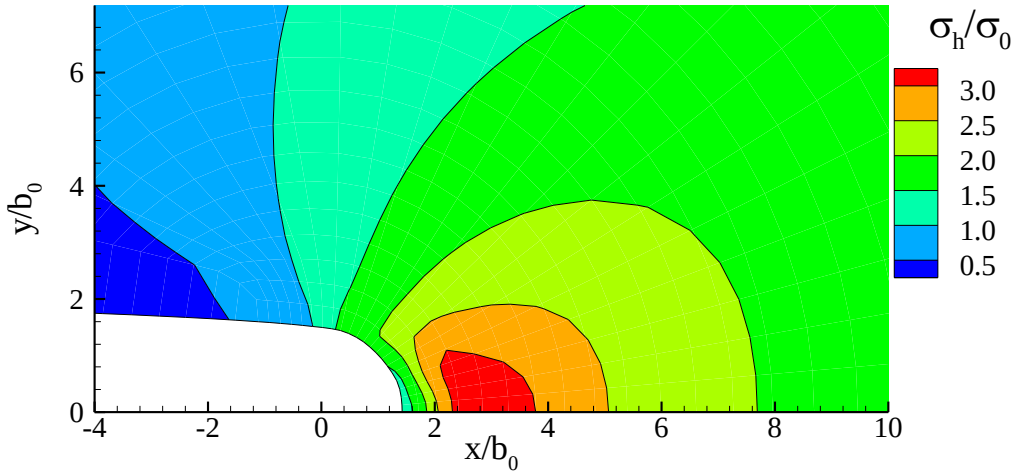

(a)

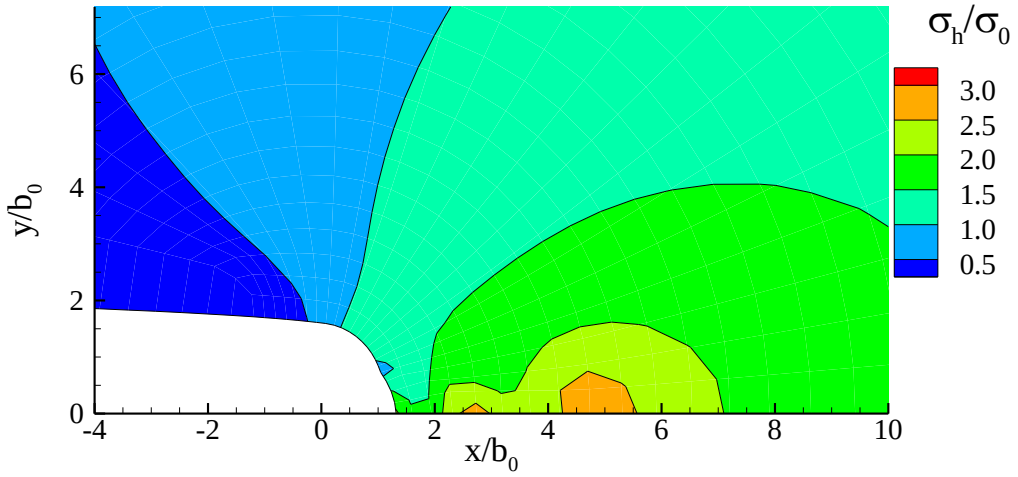

(b)

Figure 6.11: Distributions of normalized hydrostatic stress $\sigma_{\mathrm{h}}/\sigma_0$ in the crack tip vicinity for material E at $J_{\mathrm{app}}/(\sigma_0 b_0) = 2.25$. a) Plastically incompressible solid, $\alpha_{\mathrm{p}} = 0.333333$.b) Plastically compressible solid, $\alpha_{\mathrm{p}} = 0.28$

Figure 6.11 shows the corresponding hydrostatic stress distributions. For the plastically incompressible solid, $\alpha_{\mathrm{p}} = 0.333333$, in Fig.6.11a, the peak hydrostatic tension occurs at $x/b_0 \approx 3$, which is about the same location as for the hardening material in Fig. 6.9b. However, for material E, because of the softening, the stress level on the crack tip surface is reduced. With $\alpha_{\mathrm{p}} = 0.28$, Fig. 6.11b, the hydrostatic stress distribution is qualitatively different from that for the incompressible solid in Fig. 6.11a. There are two regions along the symmetry plane where there is a local peak in σ_{h}; a smaller region at $x/b_0 = 3$ and a larger region centered at $x/b_0 \approx 5$. Due to plastic compressibility the magnitude of these hydrostatic tension peaks is smaller than for the plastically incompressible solid.

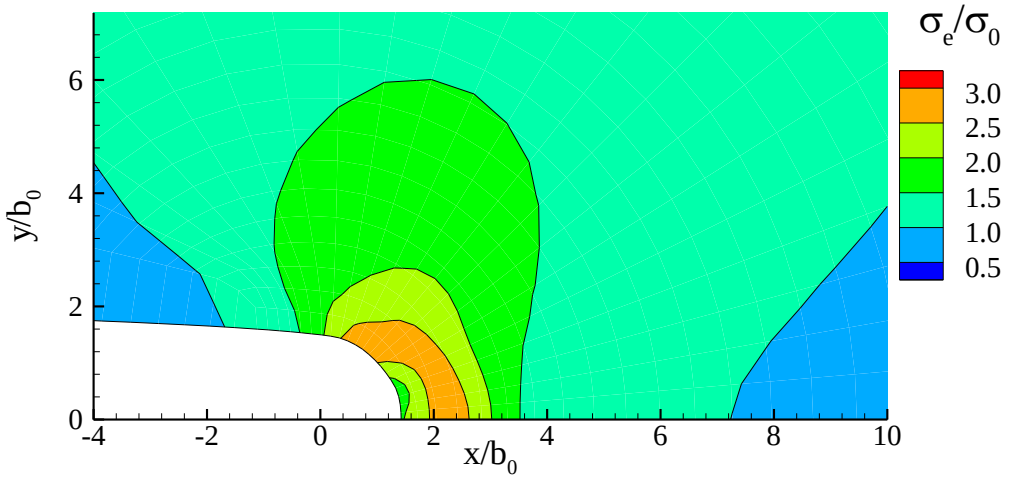

(a)

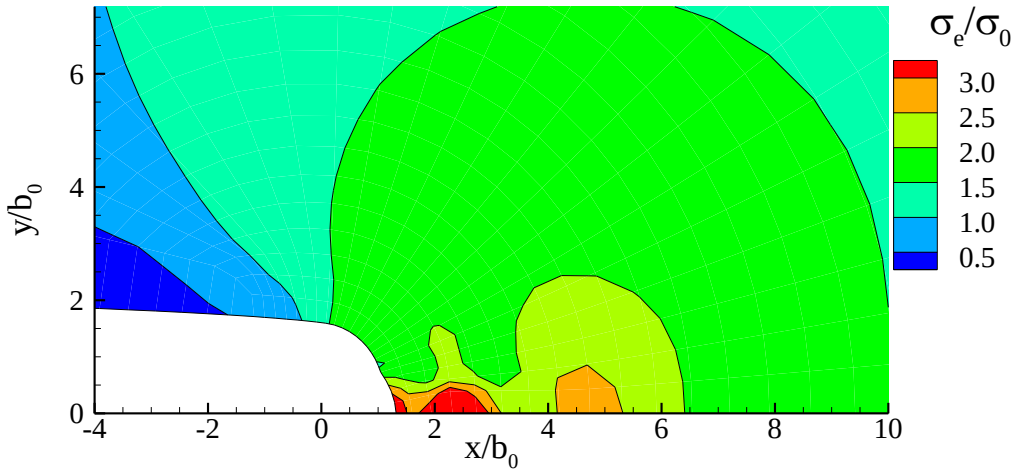

(b)

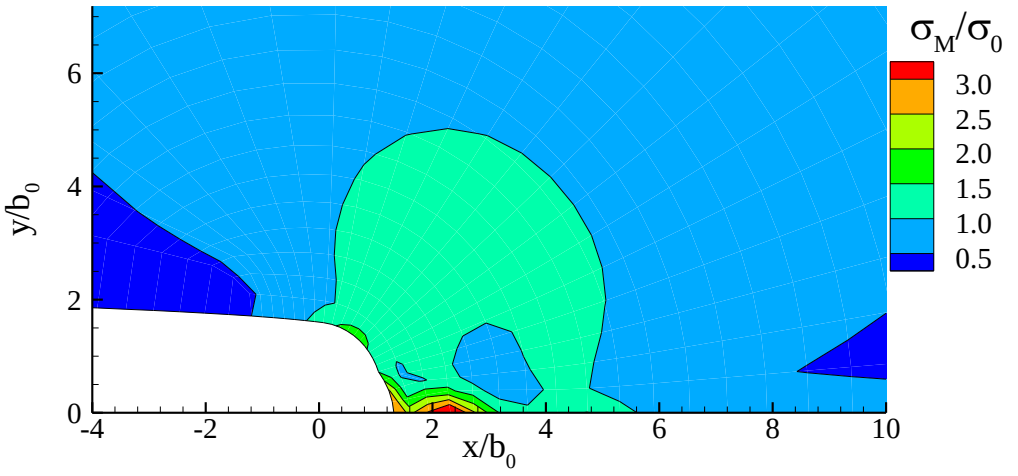

(c)

Figure 6.12: Distributions of normalized effective stress measures in the crack tip vicinity for material E at $J_{\text{app}}/(\sigma_0 b_0) = 2.25$. a) $\sigma_{\text{e}}/\sigma_0$ for a plastically incompressible solid, $\alpha_{\text{p}} = 0.333333$. b) $\sigma_{\text{e}}/\sigma_0$ for a plastically compressible solid, $\alpha_{\text{p}} = 0.28$. c) $\sigma_{\text{M}}/\sigma_0$ for a plastically compressible solid, $\alpha_{\text{p}} = 0.28$

Next, distributions of the work conjugate effective stress, σ_e defined by Eq. (4.7), are shown in Fig. 6.12a, b. For the plastically incompressible solid in Fig. 6.12a, the band of increased σ_e overlaps the band of increased straining in Fig.6.8a. The increased σ_e and increased ε_p occur in similar regions because the value of ε_p away from the notch surface is less than 0.4 so that the local minimum value of g (which occurs at $\varepsilon_p = 0.6$) has not yet been reached. In Fig. 6.12b, the values of ε_p directly in front of the crack tip exceed 0.7 and so the material in this region is on the rehardening branch of g. There is another region of increased σ_e near $x/b_0 = 5$ due to the dependence of σ_e on the hydrostatic stress σ_h. Thus, in contrast to the case for the hardening Mises material, there is a region where both σ_h and σ_e attain increased values. However, note that there is not a substantial increase in ε_{vol} in Fig. 6.10c associated with the region around $x/b_0 = 5$ where there is a local hydrostatic stress peak.

For a plastically incompressible solid as in Fig.6.12a, σ_e and the Mises effective stress, σ_M in Eq. (4.11), are equal. However, for a plastically compressible solid these effective stress measures differ significantly as seen by comparing Fig. 6.12b, c. This comparison shows that in front of the crack tip along the crack plane, where the large values of ε_p occur in Fig. 6.10b, and both σ_e and σ_M are large, there is a significant hydrostatic stress contribution to σ_e. The distribution of σ_M for the plastically compressible solid differs substantially from that for the plastically incompressible solid in Fig.6.12a.

It is also worth noting that calculations were carried out for material E using a 22 × 54 element mesh and the distributions obtained with that coarser mesh agreed well with the distributions of ε_p, ε_{vol} and σ_h/σ_0 shown in Figs. 6.10 – 6.12 where a 22 × 64 element mesh was used. Of course, when a very localized deformation field develops ahead of the crack tip

as in Figs. 6.10b, c, the mesh spacing sets the minimum width of the region of localized deformation. In addition, a much finer mesh resolution than used here would be needed to resolve any complex deformation pattern that may be associated with highly localized deformation in the crack tip region, as seen, for example, in Ref. (Lai and van der Giessen, 1997). Nevertheless, the occurrence of a localized region of deformation for a plastically compressible hardening–softening–hardening material but not for a corresponding incompressible material, as well as the consequences, if any, for the J_{app} versus $(b/b_0 - 1)$ response and the plastic zone size and shape, are revealed by the mesh resolutions used here.

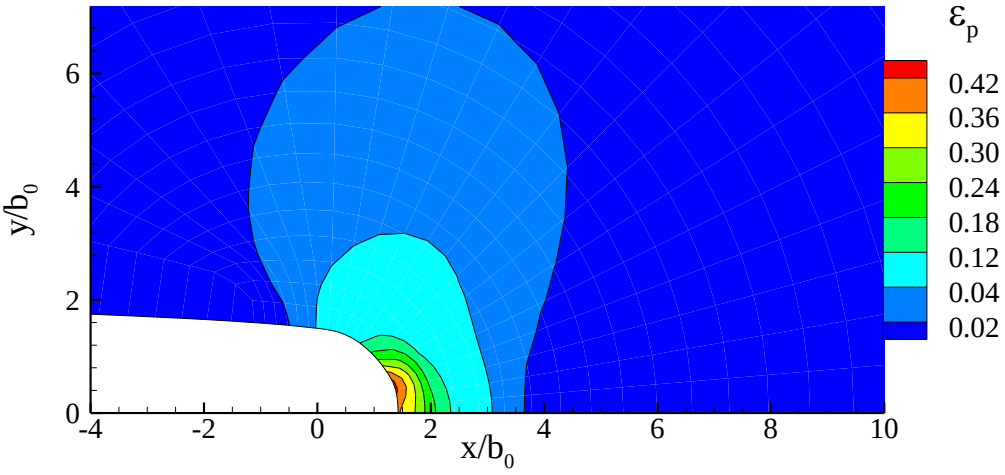

(a)

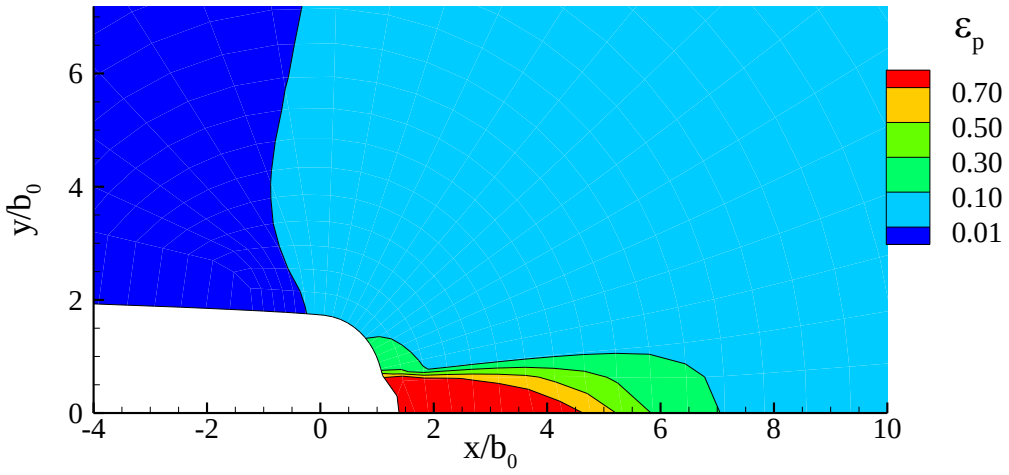

(b)

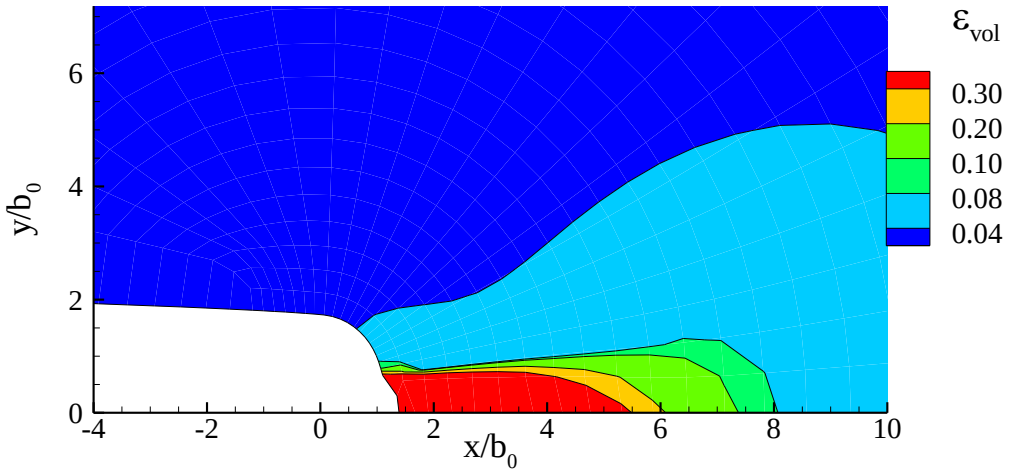

(c)

Figure 6.13: Distributions of plastic strain, ε_{p} in the crack tip vicinity for material G at $J_{\mathrm{app}}/(\sigma_0 b_0) = 2.25$.a) Plastically incompressible solid, $\alpha_{\mathrm{p}} = 0.333333$.b) Plastically compressible solid,$\alpha_{\mathrm{p}} = 0.28$.c) Distribution of $\varepsilon_{\mathrm{vol}}$ for a plastically compressible solid, $\alpha_{\mathrm{p}} = 0.28$

Now, distributions of ε_p, σ_h, and σ_e for material G are shown in Figs. 6.13–6.15. Rehardening for material G takes place for $\varepsilon_p = 5.0$ and so rehardening for material G does not occur in the calculations here. The plastic strain distributions in Fig. 6.13 are qualitatively similar to those for material E in Fig. 6.10, but there are significant quantitative differences, mainly for the compressible solid in Fig. 6.13b. The large strain region in front of the crack tip extends to about $x/b_0 = 5$ versus $x/b_0 = 3$ for material E. As a consequence of these large strains the crack surface has a clear V-like wedge shape near the symmetry plane. In Fig. 6.13b, c, as in Fig. 6.10b, c, the minimum width of the highly deformed regions is set by the finite element mesh.

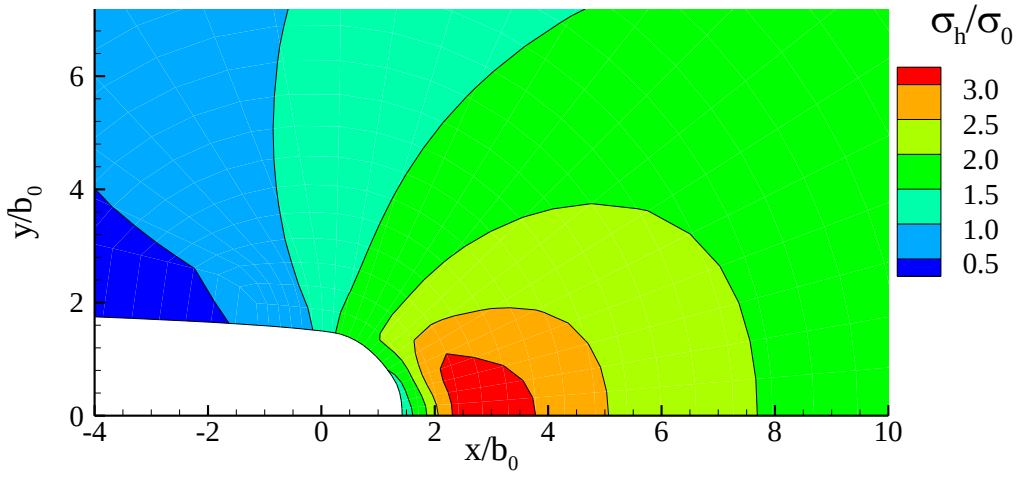

(a)

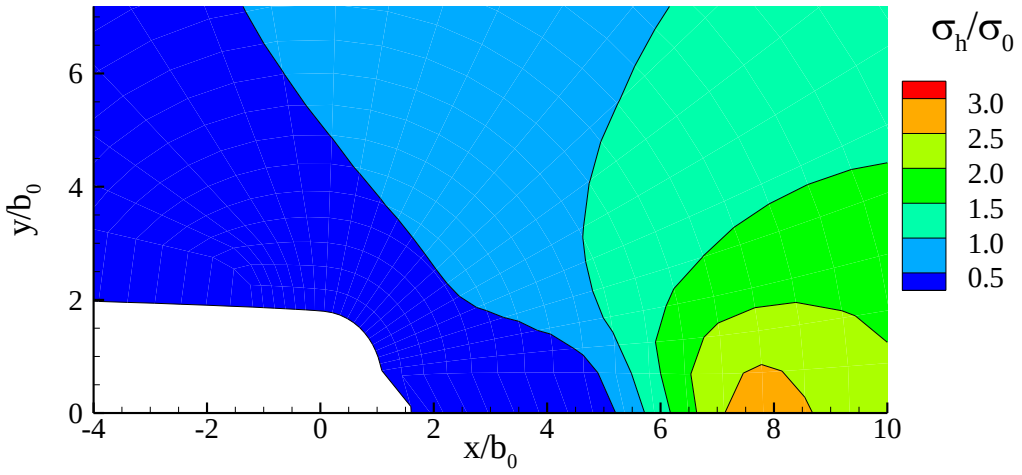

(b)

Figure 6.14: Distributions of normalized hydrostatic stress $\sigma_{\mathrm{h}}/\sigma_0$ in the crack tip vicinity for material G at $J_{\mathrm{app}}/(\sigma_0 b_0) = 2.25$. a) Plastically incompressible solid, $\alpha_{\mathrm{p}} = 0.333333$.b) Plastically compressible solid, $\alpha_{\mathrm{p}} = 0.28$

For the plastically incompressible solid, the distribution of σ_{h} in Fig. 6.14a is similar to that in Fig. 6.11a for material E. On the other hand, with $\alpha = 0.28$ in Fig. 6.14b, the hydrostatic tension is now low in front of the crack tip and the region of a local peak σ_{h} has moved out to $x/b_0 = 8$.

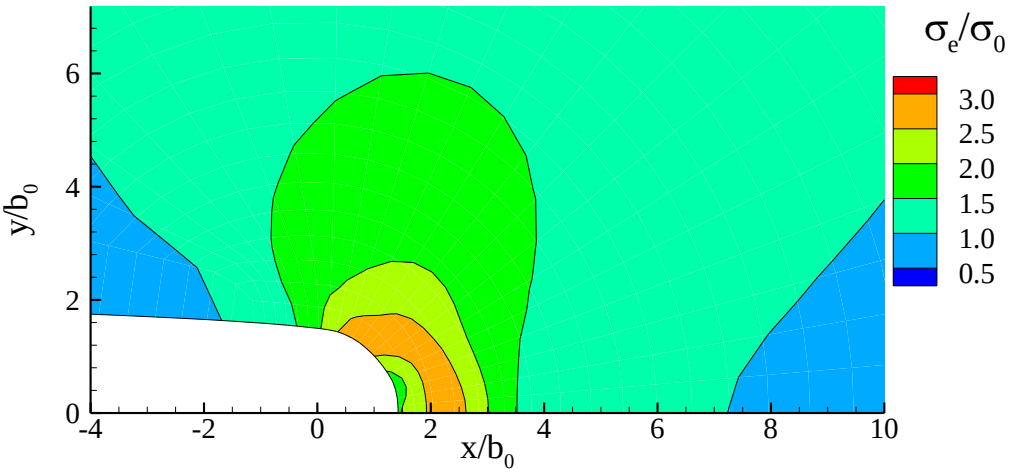
σe/σ0
3.0
2.5
2.0
1.5
1.0
0.5
y/b0
x/b0
0
2
4
6
-4
-2
0
2
4
6
8
10

(a)

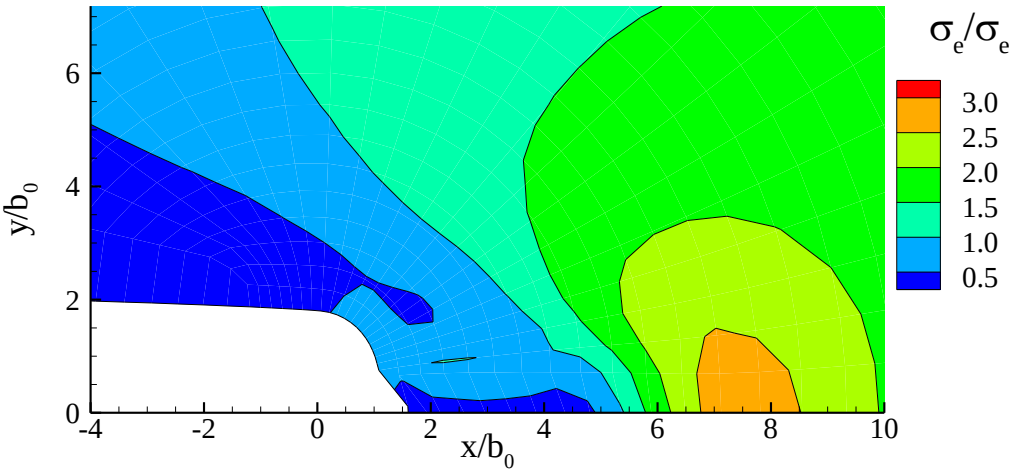
σe/σe
3.0
2.5
2.0
1.5
1.0
0.5
y/b0
x/b0
0
2
4
6
-4
-2
0
2
4
6
8
10

(b)

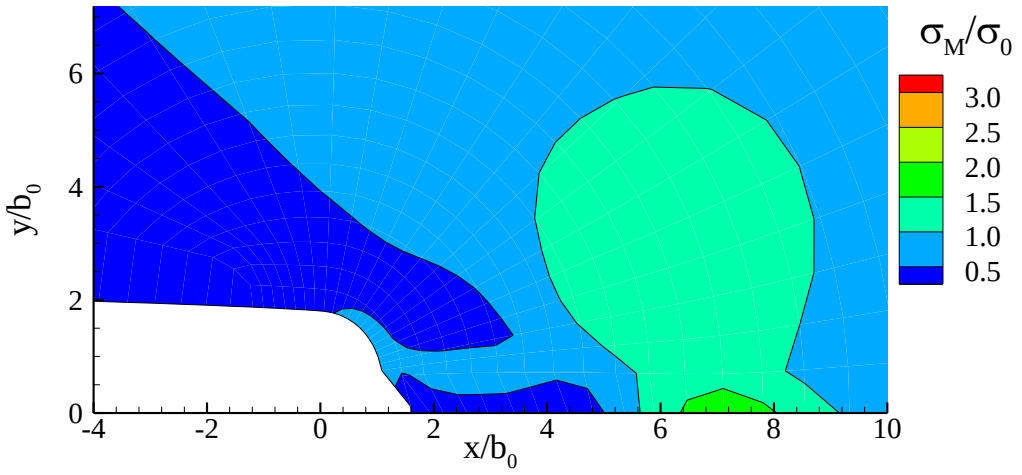

(c)

Figure 6.15: Distributions of normalized effective stress measures in the crack tip vicinity for material G at $J_{app}/(\sigma_0 b_0) = 2.25$. a) σ_e/σ_0 for a plastically incompressible solid, $\alpha_p = 0.333333$ .b) σ_e/σ_0 for a plastically compressible solid, $\alpha_p = 0.28$. c) σ_M/σ_0 for a plastically compressible solid, $\alpha_p = 0.28$

As for σ_h, the lack of rehardening has the greatest effect on the distribution of σ_e for the plastically compressible solid in Fig.6.15b. Because of the softening with no rehardening for material G, the values of σ_e are low in front of the crack tip where the values of ε_p are large. There is a region of locally high values of σ_e at about $x/b_0 = 8$, which is also where the local peak in hydrostatic stress is located. Thus, for both material E and material G the regions of increased hydrostatic tension and effective stress overlap. The rehardening (or lack of rehardening) affects the value of x/b_0 at which this region of increased stress occurs.

It should be mentioned here that for amorphous glassy polymer (where there is intrinsic softening just after the yield and thereafter subsequent orientational strain hardening) similar kind of finite element finite deformation studies (as well as micromechanically motivated

studies) were done by Lai and Van der Giessen (1997), Basu and Van der Gissen (2002) etc. for plastically incompressible solids. Even though the plastic zones in glassy polymers are completely different in shape than those from the present materials, similar phenomena like strain localization, shear banding, continuous propagation of the plastic zone etc are observed in those cases also.

6.5 Some Results under Cyclic Loading (Plastic Normality Condition)

Now the same geometry and constitutive equation are again considered, however K_{I} field displacements expressed in section 6.2 and which is imposed on the semi-circular boundary would be cycled corresponding to $(K_{\mathrm{I}})_{\max}$ and $(K_{\mathrm{I}})_{\min}$.

6.5.1 Crack-tip Deformation

By plastic blunting we mean crack growth due to the crack tip opening and for small scale yielding, usually the crack extension per cycle is described in terms of ΔK. Though there are several definitions of CTOD, here we have used it as $\delta_{\mathrm{t}} = b/b_0 - 1$, where b is the current crack opening at $x = -0.004$; and this CTOD can be used to characterize the near-tip fracture process zone. In order to reflect the effect of ΔK, R, N, α and material softening on CTOD, we have plotted the variation of CTOD with respect to applied normalized constant amplitude loading J_{app} (=$K_{\mathrm{I}}^2(1-v^2)/E$), Figs. 6.16 – 6.21. Ten complete load cycles have been considered for the loading regimes. For material B, during the 1st loading cycle, the parabolic curve represents that the crack opening is initially dominated by elastic deformation. Cyclic trajectories appear to be dependent on $K_{\max}$ and $K_{\min}$, R, α_{p} and they are influenced by N as well. It is noticeable that when material is plastically compressible and ΔK is rising, CTOD increases significantly and convergence of the CTOD – trajectories

to the steady-state and self-similar loops gets delayed. Ratcheting of CTOD – trajectories diminishes with rising N, and they converge gradually to steady-state and self-similar loops. This has been shown clearly in Fig. 6.17 and Fig. 6.20 using "in set" enlarged view. When R is positive (here it is 0.33), the CTOD – trajectories converge to the steady-state and self-similar loops very quickly for both plastically incompressible and compressible solids, Fig. 6.18. On the other hand, for material E, the observed CTOD is more as compared to that of the material B. When material E is plastically compressible, in the first loading cycle there are more or less abrupt jumps and these jumps are dependent on $K_{\max}$ and $K_{\min}$, R. These jumps are associated with the evolution of a region of localized deformation (as will be shown subsequently) that develops in front of the initial crack tip for material E with α =0.28 but not when the material is incompressible. The increase of CTOD with the J_{app} for both the materials may be attributed to the development of localized deformation region near to the crack tip when the material is plastically compressible. When R is zero and material E is plastically compressible the convergence of CTOD – trajectories to the steady-state and self-similar loops is slow. It is also visible that at higher $K_{\max}$ even when the material E is plastically incompressible some jumps are observed in the first CTOD trajectory. Localized deformation due to compressibility as well as material softening as observed later may be the reason behind this. Like material B, here also for R positive, the convergence of the CTOD – trajectories is very fast.

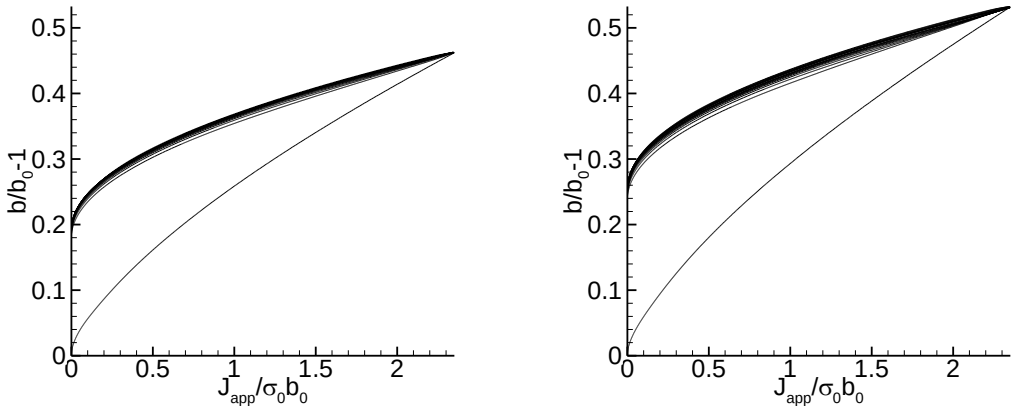

(a) (b)

Figure 6.16: Crack-tip opening displacement $\delta_t(= b/b_0 - 1)$ versus applied *J*-integral, J_{app} in material B with $K_{max} = 0.5$ and $K_{min} = 0$; a) Plastically incompressible solid b) Plastically compressible solid, $\alpha_p = 0.28$ (up to 10th cycle)

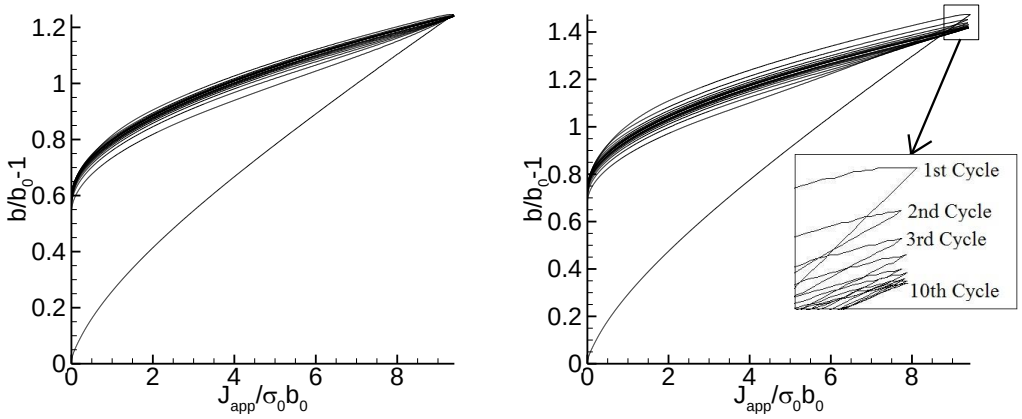

(a) (b)

Figure 6.17: Crack-tip opening displacement $\delta_t(= b/b_0 - 1)$ versus applied *J*-integral, J_{app} in material B with $K_{max} = 1.0$ and $K_{min} = 0$; a) Plastically incompressible solid b) Plastically compressible solid, $\alpha_p = 0.28$ (up to 10th cycle)

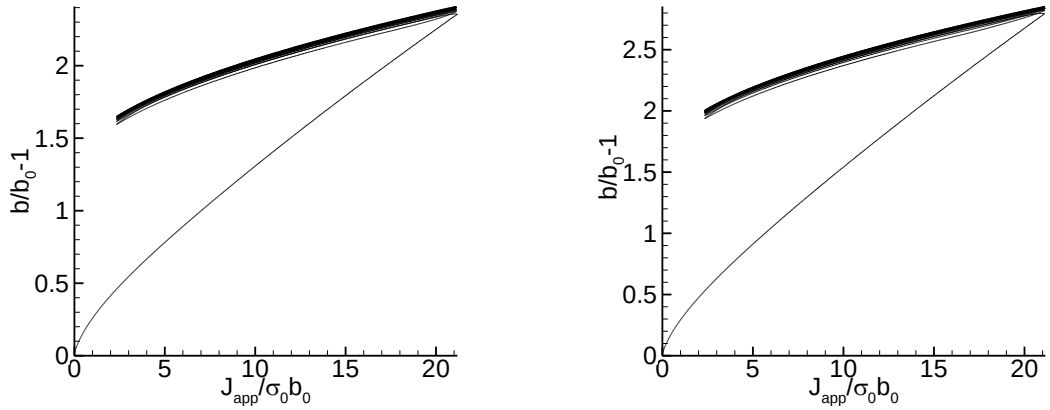

(a) (b)

Figure 6.18: Crack-tip opening displacement $\delta_t(= b/b_0 - 1)$ versus applied *J*-integral, J_{app} in material B with $K_{max} = 1.5$ and $K_{min} = 0.5$; a) Plastically incompressible solid b) Plastically compressible solid, $\alpha_p = 0.28$ (up to 10^{th} cycle)

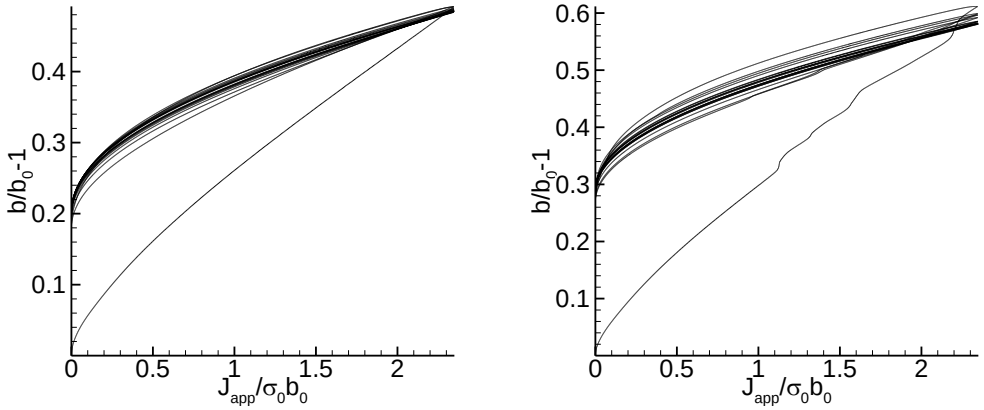

(a) (b)

Figure 6.19: Crack-tip opening displacement $\delta_t(= b/b_0 - 1)$ versus applied *J*-integral, J_{app} in material E with $K_{max} = 0.5$ and $K_{min} = 0$; a) Plastically incompressible solid b) Plastically compressible solid, $\alpha_p = 0.28$ (up to 10^{th} cycle)

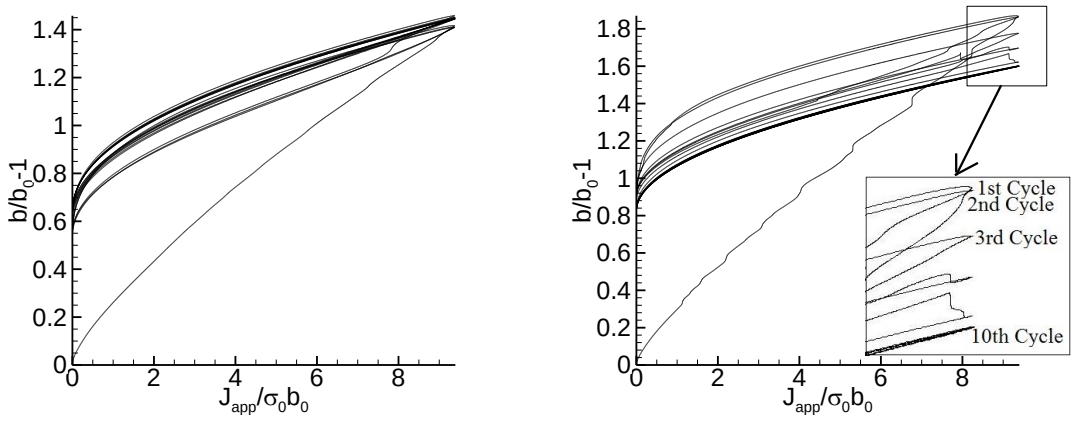

(a) (b)

Figure 6.20: Crack-tip opening displacement $\delta_t(= b/b_0 - 1)$ versus applied *J*-integral, J_{app} in material E with $K_{max} = 1.0$ and $K_{min} = 0$; a) Plastically incompressible solid b) Plastically compressible solid, $\alpha_p = 0.28$ (up to 10th cycle)

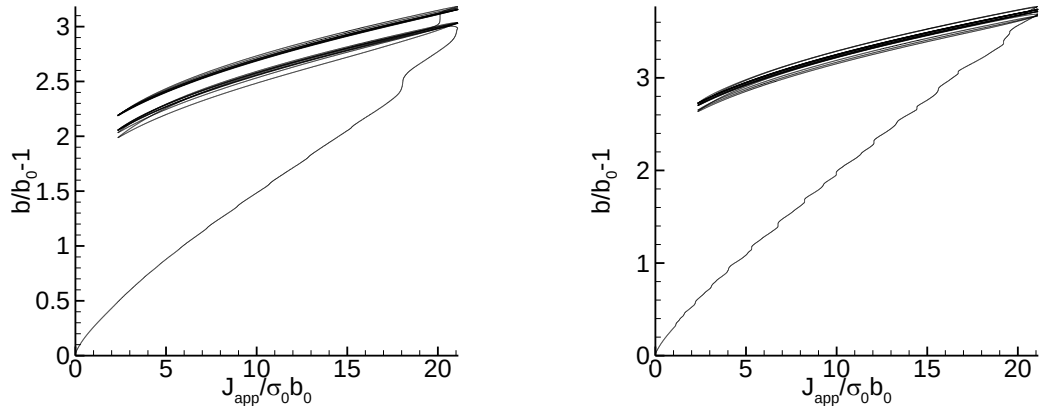

(a) (b)

Figure 6.21: Crack-tip opening displacement $\delta_t(= b/b_0 - 1)$ versus applied *J*-integral, J_{app} in material E with $K_{max} = 1.5$ and $K_{min} = 0.5$; a) Plastically incompressible solid b) Plastically compressible solid, $\alpha_p = 0.28$ (up to 10th cycle)

In order to reflect the effect of overloading on CTOD , we have plotted again the variation of CTOD with respect to applied normalized loading, Figs. 6.22 – 6.23. The overload was applied on the fifth cycle and it's amount has been specified in section 6.2. It is visible here that for both the materials B and E, in comparison with the pre-overload CTOD loops, the post-overload CTOD loops shift upwards depending on the magnitude of $K_{overload}$ but preserving the shape and size of the former loops. In material E where there is a material softening, during the overload cycle abrupt jumps in the CTOD plot is observed. This abrupt jumps are associated with the evolution of a region of localized deformation that develops in front of the initial crack tip for material E. CTODs are still higher when the material is plastically compressible. Thus under constant amplitude loading regimes, whether or not interrupted by overload, the CTOD trajectories acquire fairly steady-state loop patterns.

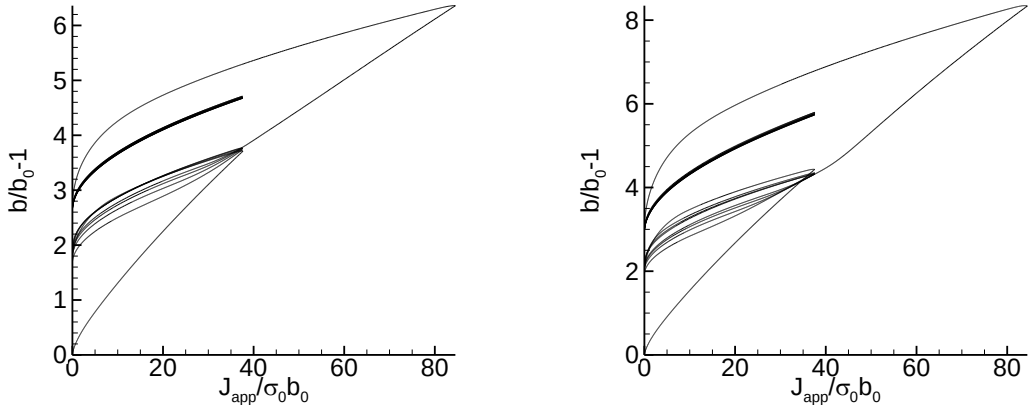

(a) (b)

Figure 6.22: Crack-tip opening displacement $\delta_t(= b/b_0 - 1)$ versus applied *J*-integral, J_{app} in material B with $K_{max} = 2.0$ and $K_{min} = 0$; a) Plastically incompressible solid b) Plastically compressible solid, $\alpha_p = 0.28$, with overload, (up to 10^{th} cycle)

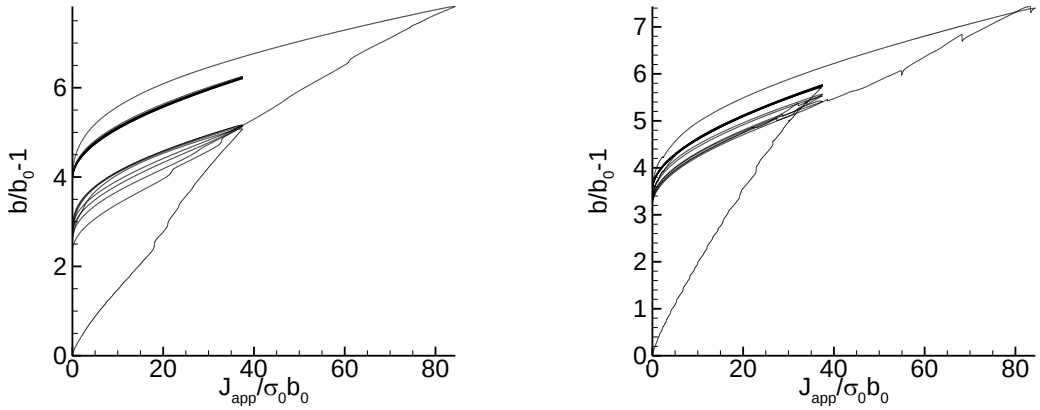

(a) (b)

Figure 6.23: Crack-tip opening displacement $\delta_t(= b/b_0 - 1)$ versus applied *J*-integral, J_{app} in material E with $K_{max} = 2.0$ and $K_{min} = 0$; a) Plastically incompressible solid b) Plastically compressible solid, $\alpha_p = 0.28$, with overload, (up to 10^{th} cycle)

In order to observe how the crack tip blunting model works, now, deformation patterns near the crack tip are plotted at the end of loading and unloading phases of the fifth cycle (for the loading regime $K_{max} = 2.0$ and $K_{min} = 0$) separately for plastically incompressible and compressible solids in Figs. 6.24 – 6.27. It is reflected that for material B, the crack profiles at low-peak load are like the keyhole shapes tapering in the wake region behind the tip for plastically incompressible solid and for plastically compressible solid the crack profiles are tapering in the wake region behind the tip along with a sharp v-shape at the crack tip. Crack profiles were also captured for the other loading regimes and the pattern observed was of similar in nature. Also it is to be noted here that the crack width not at all returned to its initial value for all the load cases and there was no crack closure observed. For the finite strain analysis of blunting, finite element mesh with a small initial rounding of the crack tip was used and therefore, this may explain why crack closure was not there during the load

removal. The incompressible results agree also with small-deformation analysis as well as with similar finite deformation modeling (Kharin and Toribio, 2009; Levkovitch et al., 2005). This is to mention here that yielding occurs during both loading and unloading phases. On the other hand in case of material E (where the hardness function is of hardening-softening-hardening type), the simulation yielded crack extension by the progressive large deformations and like material B, resharpening during the unloading phase of the loading cycle is very significant. However, the crack tip shapes are completely different during both loading and unloading as compared to those of material B, Figs 6.26 – 6.27. When the material E is plastically incompressible there is wavy notch boundary and for plastically compressible material E, the crack tip is very much blunt in nature and this makes the crack propagation difficult which would be shown later. It is inferred that both material softening and plastic compressibility are responsible for this wavy notch boundary as well as much blunt crack tip. It is noticeable that mesh deformation is still within the limit for both the materials. In absence of remeshing results are now provided only up to a few load cycles; however the study with remeshing is under way.

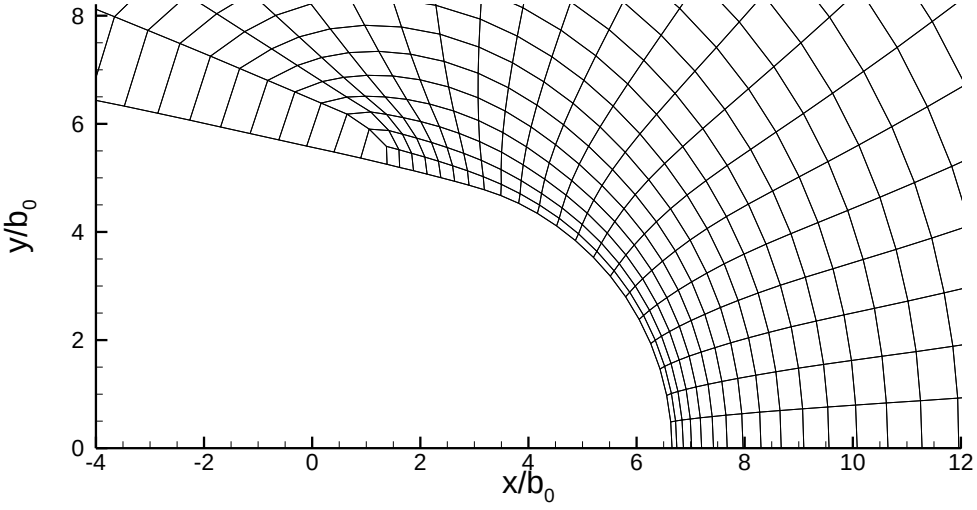

(a)

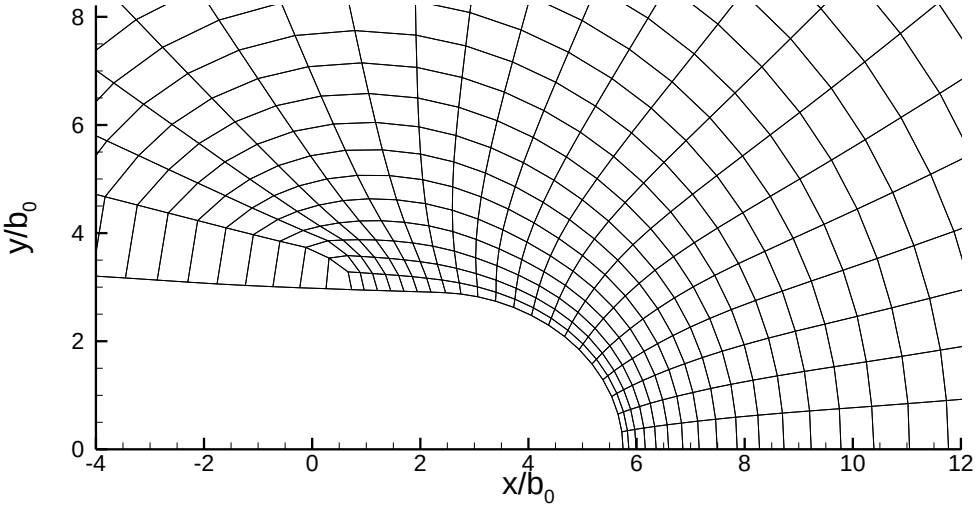

(b)

Figure 6.24: Crack-tip deformations for plastically incompressible solid, material B, $K_{\max} = 2.0$ and $K_{\min} = 0$; a) At the end of loading phase, $K \rightarrow K_{\max}$ b) At the end of unloading phase, $K \rightarrow K_{\min}$ for 5^{th} cycle

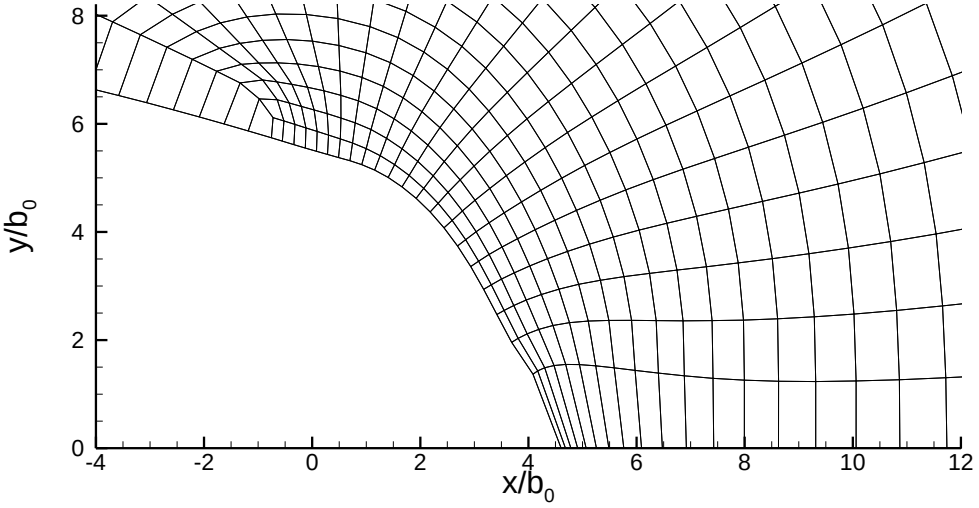

(a)

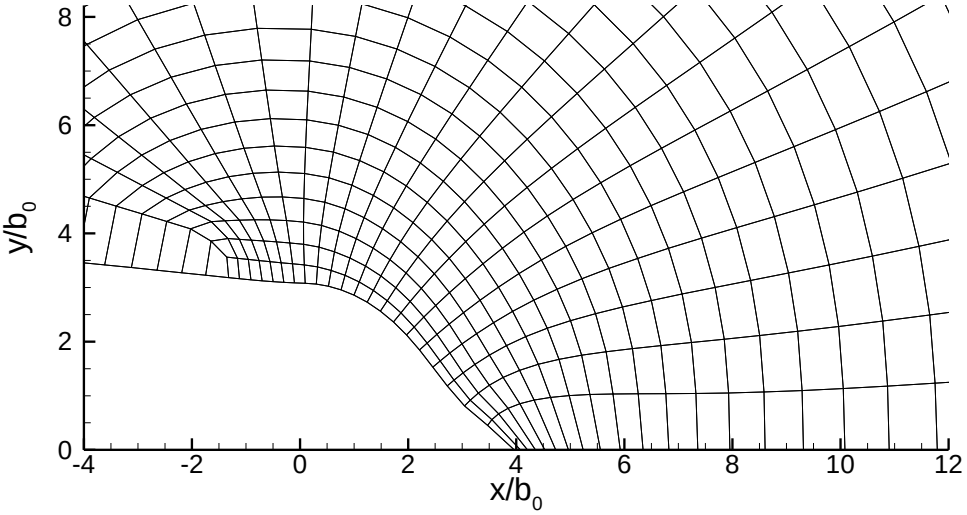

(b)

Figure 6.25: Crack-tip deformations for plastically compressible solid, material B, $\alpha_{\mathrm{p}} = 0.28$, $K_{\max} = 2.0$ and $K_{\min} = 0$; a) At the end of loading phase, $K \rightarrow K_{\max}$ b) At the end of unloading phase, $K \rightarrow K_{\min}$ for 5^{th} cycle

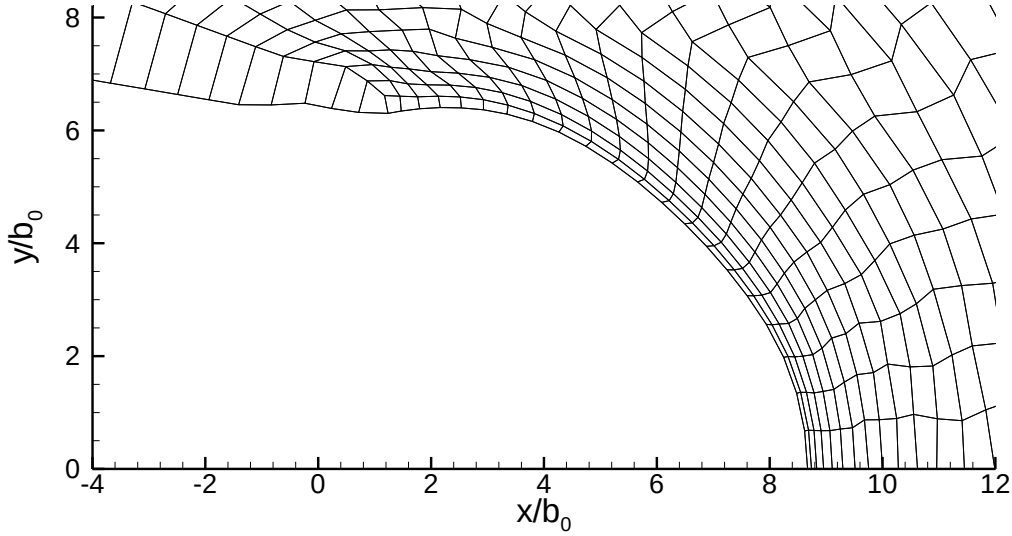

(a)

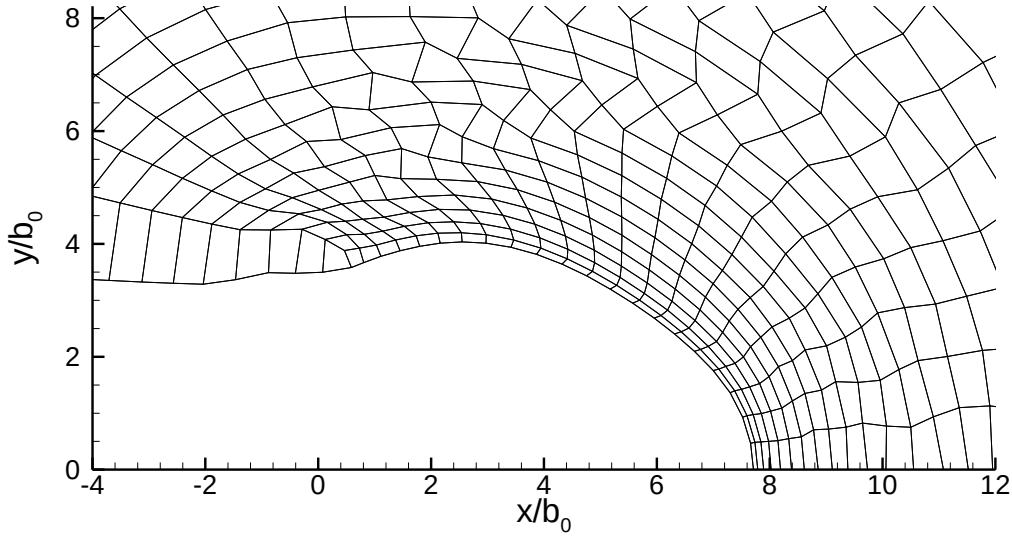

(b)

Figure 6.26: Crack-tip deformations for plastically incompressible solid, material E, $K_{\max} = 2.0$ and $K_{\min} = 0$; a) At the end of loading phase, $K \rightarrow K_{\max}$ b) At the end of unloading phase, $K \rightarrow K_{\min}$ for 5^{th} cycle

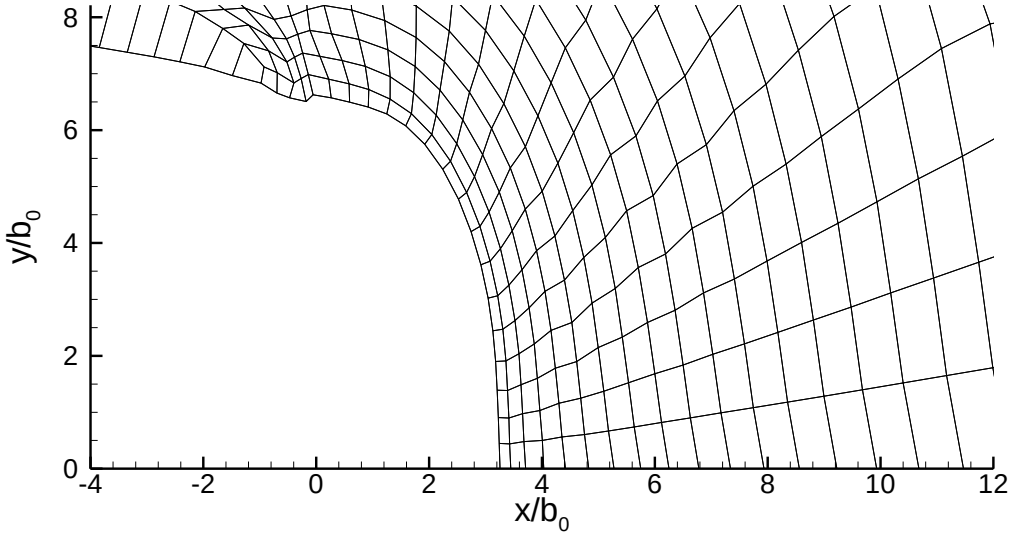

(a)

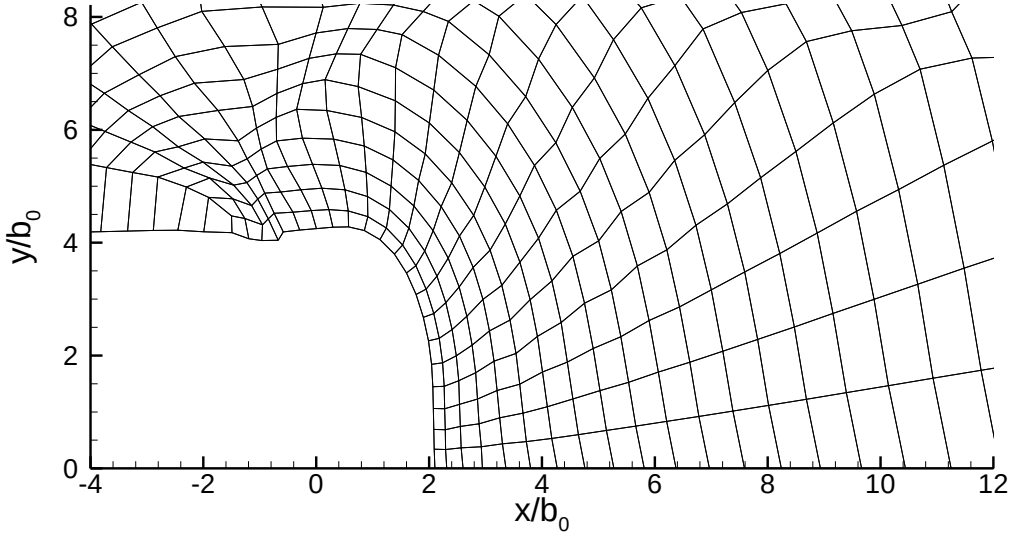

(b)

Figure 6.27: Crack-tip deformations for plastically compressible solid, material E, $\alpha_{\mathrm{p}} = 0.28$, $K_{\max} = 2.0$ and $K_{\min} = 0$; a) At the end of loading phase, $K \rightarrow K_{\max}$ b) At the end of unloading phase, $K \rightarrow K_{\min}$ for 5^{th} cycle

Another feature of crack tip deformation is plastic crack tip advancement, Δa, i.e. displacement of the crack tip apex point along the crack direction and beyond the initial crack tip location. The limitation of the present modeling strategy is that the crack growth came solely by the blunting/ resharpening mechanism as mentioned in chapter 2. For both the materials B and E, the normalized crack extension ($\Delta a/b_0$) versus normalized time (t/t_0) has been presented in Figs. 6.28 – 6.29 for constant amplitude loading. The material dependent time, t_0, that serves as a normalization time, is defined by, $t_0 = \varepsilon_0/\dot{\varepsilon}_0$, where $\varepsilon_0 (= \sigma_0/E)$ is the yield strain whose value here is 0.01. In Figs. 6.28 (a), 6.28 (b), 6.29 (a) and 6.29 (b), ΔK is varied and R is kept constant (and it is zero here) whereas in 6.28 (c), 6.28 (d), 6.29 (c) and 6.29 (d), R is positive (and it is 0.33 and 0.5 here) and varied but ΔK is kept constant. For the specified loading regimes, the crack tip advancement for a given time increases substantially with an increase in the applied stress intensity factor, as expected. However, when R value increases but ΔK is kept constant, there is increase of the crack tip advancement during the first loading cycle only and there after it is more or less remaining constant. Here, slopes in the figures provide the rates of plastic crack growth per cycle d*a*/dN, which is a function of both ΔK and *R*. In all the simulated load cases, calculated d*a*/dN from the plots is of the order of 10^{-4} unit/cycle. Here, the calculated plastic crack growth by blunting – resharpening reproduces common experimental trends of fatigue crack growth pertaining to the effects of ΔK. Crack growth is maximum in plastically incompressible material E. The highest da/dN occurs during the first loading cycle, drops significantly, and becomes relatively constant for both plastically incompressible and compressible solids. The relative increase of crack tip advancement is more when the material is plastically incompressible; however, the growth is very less when the material is plastically compressible and in presence of plastic

compressibility and material softening the crack growth is further reduced. The compressibility and material softening reduce the crack growth to a significant level. In the last figure it was observed that the plastic compressibility and material softening made the crack tip very much blunt. It would be also shown later that the size of the plastic zone is significantly larger in plastically compressible solid as compared to that of plastically incompressible solid. Also the flow rule makes the strain localization at crack tip differently in material B and material E. Therefore, it can be ascertained that the combination of larger plastic zone (due to plastic compressibility) and material softening has reduced the plastic crack growth significantly. It should be mentioned here that for plastically incompressible solids, the nature of the fatigue crack growth shows the same initial trend as reported by others (Kharin and Toribio, 2009).

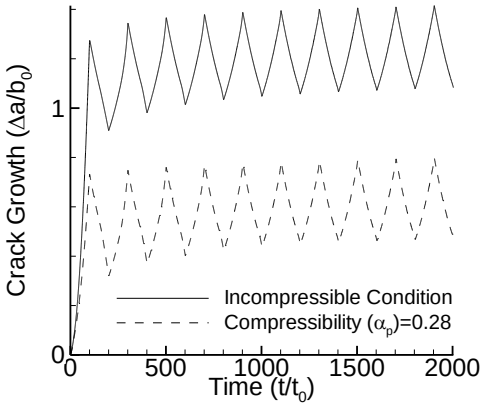

(a)

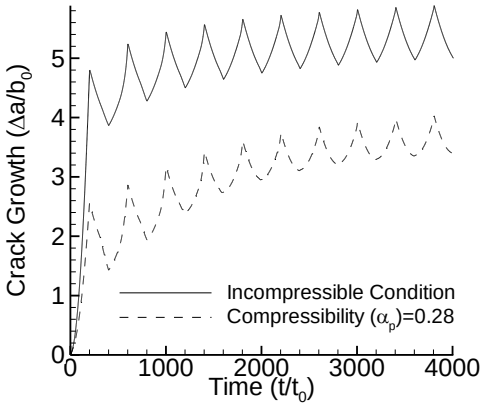

(b)

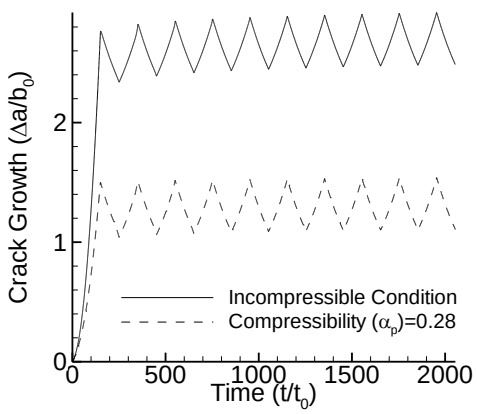

(c)

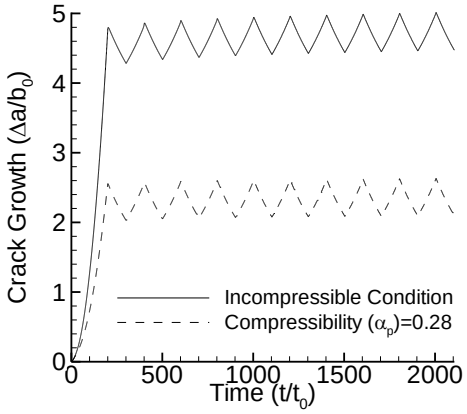

(d)

Figure 6.28: Normalized crack extension ($\Delta a/b_0$) versus normalized time (t/t_0) in plastically incompressible and compressible solids, material B; a) $K_{max} = 1.0$ and $K_{min} = 0$ b) $K_{max} = 2.0$ and $K_{min} = 0$ c) $K_{max} = 1.5$ and K_{min}=0.5 d) $K_{max} = 2.0$ and K_{min}=1.0

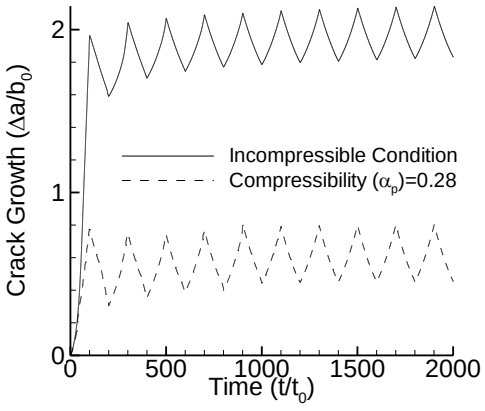

(a)

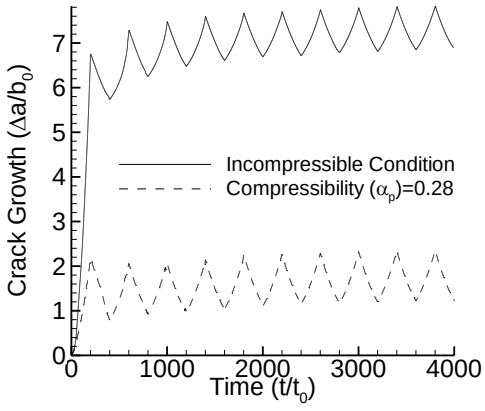

(b)

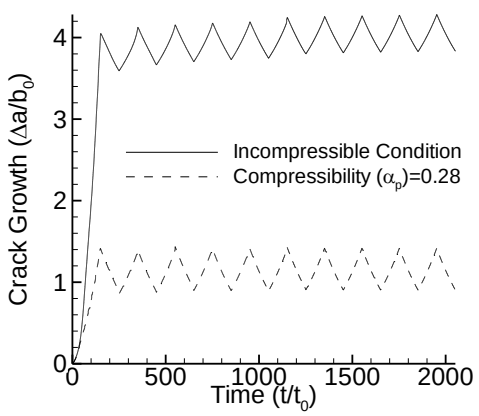

(c)

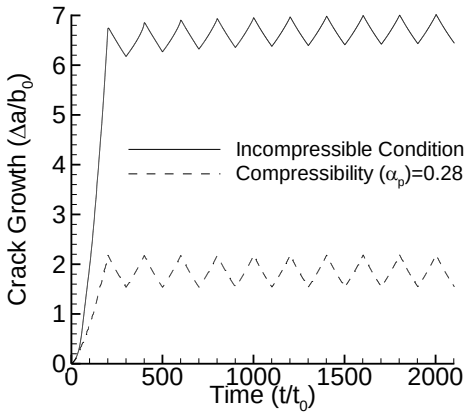

(d)

Figure 6.29: Normalized crack extension $(\Delta a/b_0)$ versus normalized time (t/t_0) in plastically incompressible and compressible solids, material E; a) $K_{max} = 1.0$ and $K_{min} = 0$ b) $K_{max} = 2.0$ and $K_{min} = 0$ c) $K_{max} = 1.5$ and K_{min}=0.5 d) $K_{max} = 2.0$ and K_{min}=1.0

Now both for materials B and E, the normalized crack extension versus normalized time in presence of overload at the fifth cycle has been presented in Figs. 6.30-6.31. It is reflected here that crack growth is sensible to an overload and this also halts the crack advance. It is very much clear that upto the 5^{th} cycle there is rising nature in the crack growth curve; during the overload the crack growth shoots up but after the overload cycle the crack growth curve is almost constant. Reason for this retarded crack growth may be the bigger plastic zone size during the application of overload which would be shown later. During the overload cycle the crack advancement is more for the plastically incompressible solid as compared to that of the plastically compressible solid. Here, again it can concluded that the combination of plastic compressibility and material softening help to reduce the crack growth significantly.

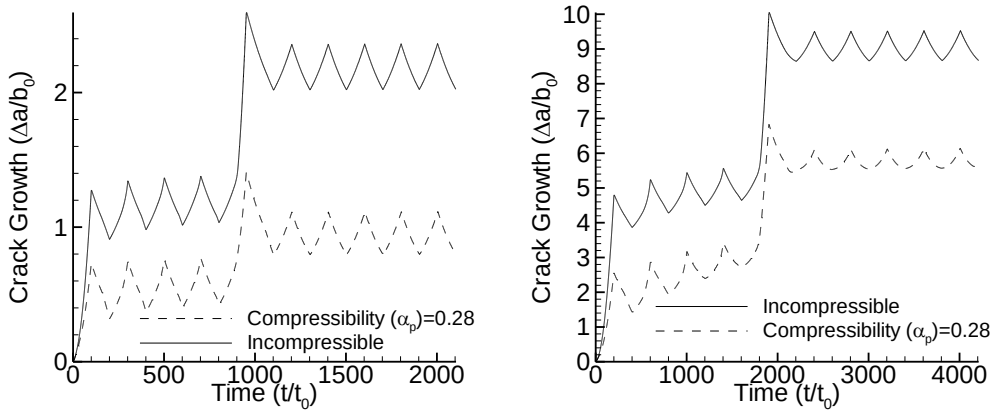

(a) (b)

Figure 6.30: Normalized crack extension $(\Delta a/b_0)$ versus normalized time (t/t_0) in plastically incompressible and compressible solids with overloading, material B; a) $K_{max} = 1.0$ and $K_{min} = 0$ b) $K_{max} = 2.0$ and $K_{min} = 0$

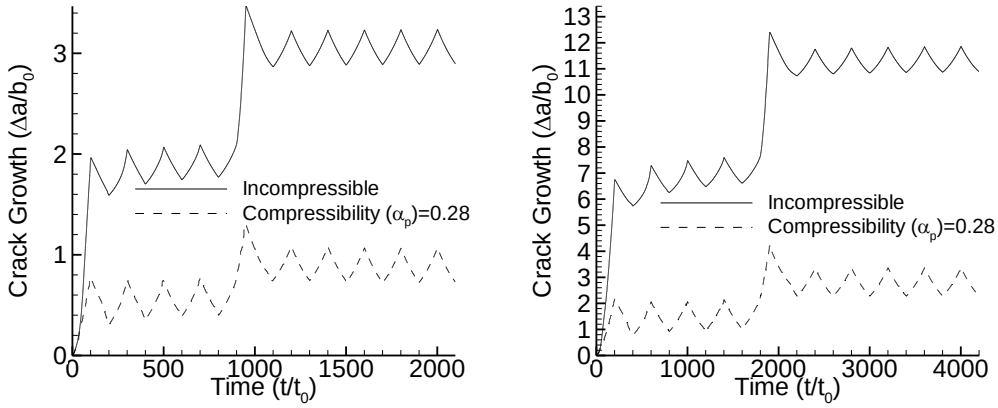

(a) (b)

Figure 6.31: Normalized crack extension $(\Delta a/b_0)$ versus normalized time (t/t_0) in plastically incompressible and compressible solids with overloading, material E; a) $K_{max} = 1.0$ and $K_{min} = 0$ b) $K_{max} = 2.0$ and $K_{min} = 0$

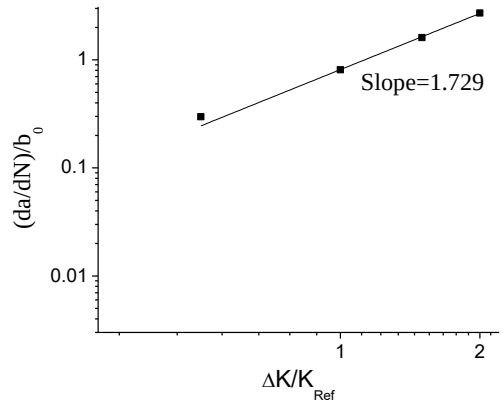

(a)

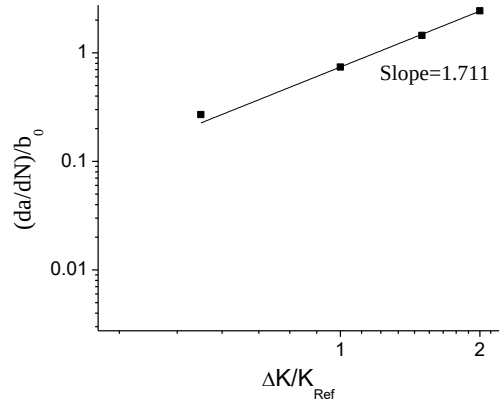

(b)

Figure 6.32: Fatigue crack growth da/dN versus ΔK for plastically compressible solids, $\alpha_{\mathrm{p}} = 0.28$, (a) Material B and (b) Material E, (with R=0) at 5^{th} cycle

In order to examine whether the present fatigue crack growth data follows the Paris power law relationship or not, we have taken out two cases here; the fatigue crack growth rates at the 5^{th} cycle for material B and material E with $\alpha_{\mathrm{p}} = 0.28$ from Figs. 6.28 and 6.29 and were replotted in terms of da/dN vs. ΔK in log-log scale and depicted in Fig. 6.32 together with the best fit line. Here again it is being mentioned that the present investigation focuses solely on

simulation of fatigue crack growth due to crack tip plasticity only. During the loading regime of the 5th load cycle the slopes of the lines were calculated. Slope was calculated using best-fit straight line to all four data points. Fig. 6.32 clearly indicates that the simulated fatigue crack growth data for constant amplitude loading (with R = 0 in this case) follows the Paris power law relationship. Here, the slope or the exponent is 1.729 for material B and, the exponent obtained for the material E is 1.711. Simulation was also done for the plastically incompressible solids, and the values of the slopes for the materials, B and E are 1.901 and 1.603, respectively. For ductile material this slope is generally in the range of 2 to 3. It can also be noted that Hunnell and Kujawski (2009), in their work reported a growth law with an exponent of 1.8898 for aluminum and they also pointed out that the amount of fatigue damage might change the fatigue crack growth rate. Here, in this work due to the lack of experimental data we are unable to validate the present exponents.

6.5.2 Plastic Zone Shape and Size

Under cyclic loading, the crack tip plastic zones have been the focus of interest as an indication of the material toughening capability. Figures 6.33 – 6.36 show distributions of plastic strain, ε_p at the end of loading and unloading phase of tenth load cycle for the loading regime $K_{max} = 1.0$ and $K_{min} = 0$ (without any overload). Figs 6.33 and 6.34 show distributions of ε_p for material B for, a plastically incompressible solid, and for a solid with α_p = 0.28, respectively. There is no difference between the plastic zone shape and size at the end of loading and unloading phase of the loading cycle for both plastically incompressible and compressible with α_p = 0.28. With α_p = 0.28, the extent of the larger strain region (ε_p > 0.01) is increased and the shape of the contours has changed from the kidney-like shape for

the plastically incompressible solid as observed in monotonic loading. The extent of plastic straining in both x and y-directions when the material is plastically compressible, is also similar to those observed in monotonic loading. Again, for both plastically incompressible solid, in Fig. 6.35, and plastically compressible solids, in Fig 6.36 where the material has a hardening–softening– hardening strength, the contours for $0.01 \geq \varepsilon_p$ are also nearly identical to those for the hardening solid in Figs. 6.32 and 6.33 like the monotonic loading.

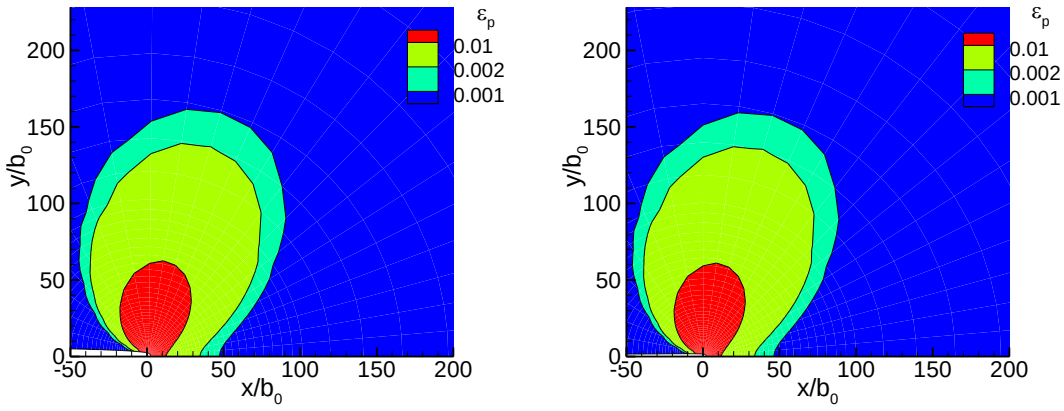

(a) (b)

Figure 6.33: Distribution of plastic strain, for plastically incompressible solid, material B, $K_{max} = 1.0$ and $K_{min} = 0$; a) At the end of loading phase, $K \rightarrow K_{max}$ b) At the end of unloading phase, $K \rightarrow K_{min}$ for 10^{th} cycle

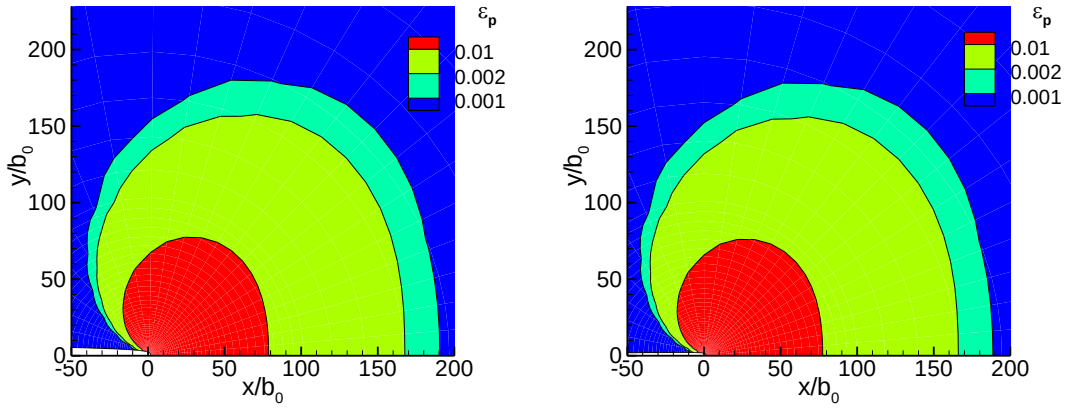

(a) (b)

Figure 6.34: Distribution of plastic strain, for plastically compressible solid, material B, $\alpha_{\mathrm{p}} = 0.28$, $\mathrm{K_{max}} = 1.0$ and $\mathrm{K_{min}} = 0$; a) At the end of loading phase, $K \rightarrow K_{\mathrm{max}}$ b) At the end of unloading phase, $K \rightarrow K_{\mathrm{min}}$ for 10^{th} cycle

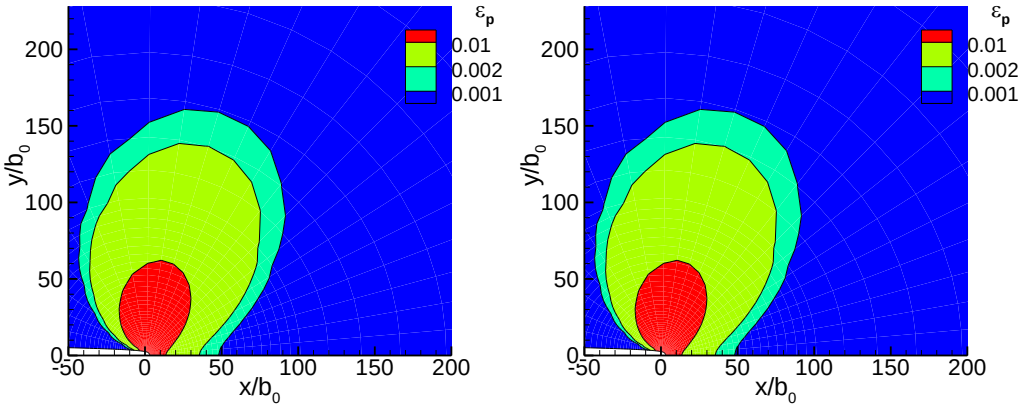

(a) (b)

Figure 6.35: Distribution of plastic strain, for plastically incompressible solid, material E, $\mathrm{K_{max}} = 1.0$ and $\mathrm{K_{min}} = 0$; a) At the end of loading phase, $K \rightarrow K_{\mathrm{max}}$ b) At the end of unloading phase, $K \rightarrow K_{\mathrm{min}}$ for 10^{th} cycle

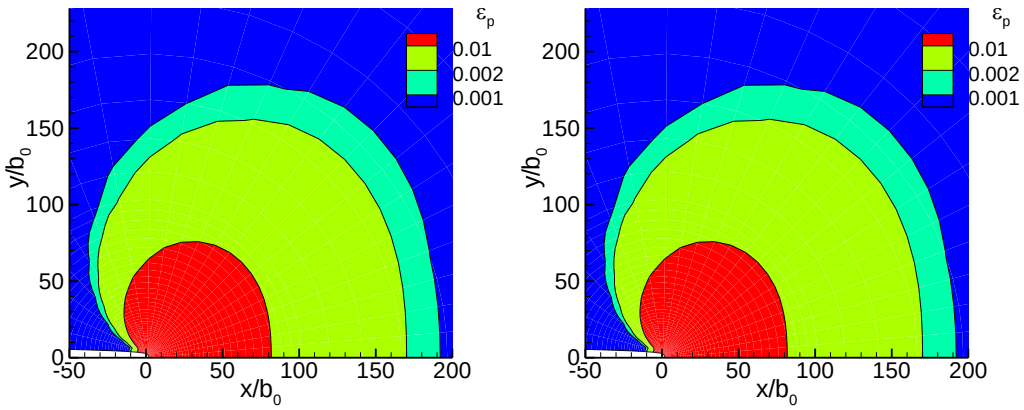

Figure 6.36: Distribution of Plastic strain, for plastically compressible solid, material E, $\alpha_{\mathrm{p}} = 0.28$, $\mathrm{K_{max}} = 1.0$ and $\mathrm{K_{min}} = 0$; a) At the end of loading phase, $K \rightarrow K_{\mathrm{max}}$ b) At the end of unloading phase, $K \rightarrow K_{\mathrm{min}}$ for 10^{th} cycle

Figures 6.37 - 6.40 illustrate the plastic zone size and shape for both the materials B and E with and without overload cycle. It is reflected here that plastic zone is very much sensitive to the overload and the loading phase of the overload cycle makes the plastic zone significantly bigger for both the materials B and E. This bigger plastic zone may explain the reason behind the crack growth retardation after the overload cycle. Also it can be noted here that the influence of the overload on the plastic zone is same to whether a material is hardening-hardening or hardening-softening-hardening.

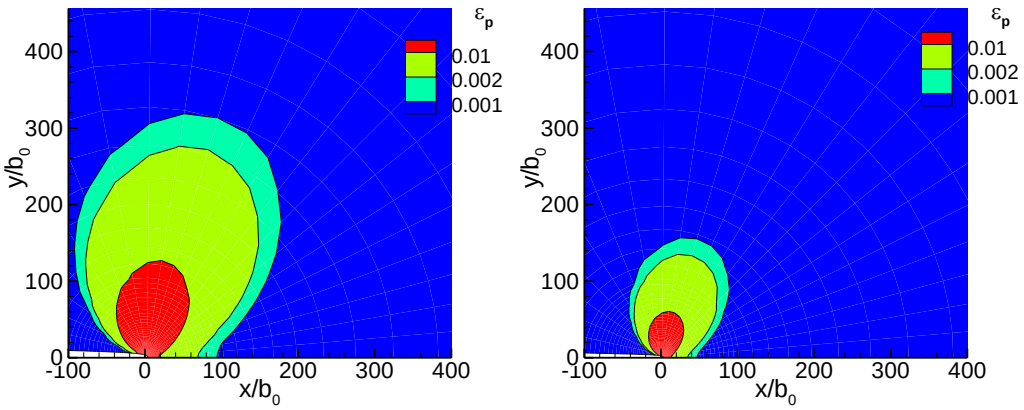

(a) (b)

Figure 6.37: Distribution of plastic strain, for plastically incompressible solid, material B, $K_{max} = 1.0$ and $K_{min} = 0$; at the end of loading phase in 5th cycle a) With overload b) Without overload

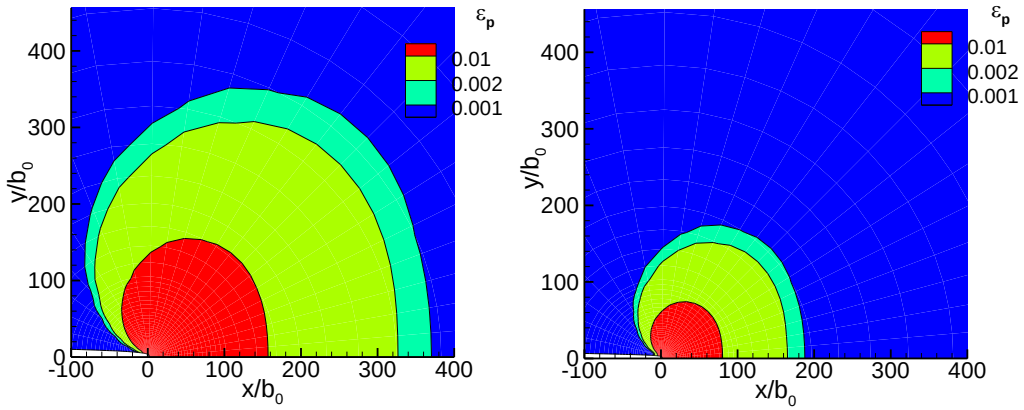

(a) (b)

Figure 6.38: Distribution of plastic strain, for plastically compressible solid, material B, $\alpha_p = 0.28$, $K_{max} = 1.0$ and $K_{min} = 0$; at the end of loading phase in 5th cycle a) With overload b) Without overload

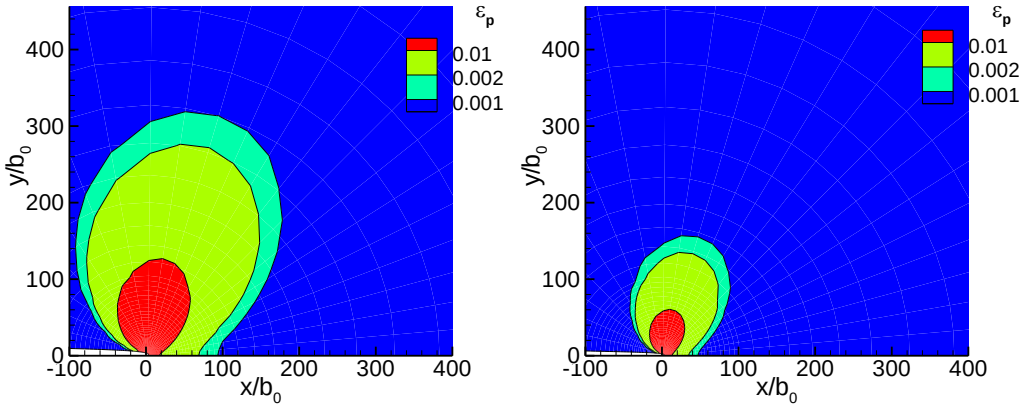

(a) (b)

Figure 6.39: Distribution of plastic strain, for plastically incompressible solid, material E, $K_{max} = 1.0$ and $K_{min} = 0$; at the end of loading phase in 5^{th} cycle a) With overload b) Without overload

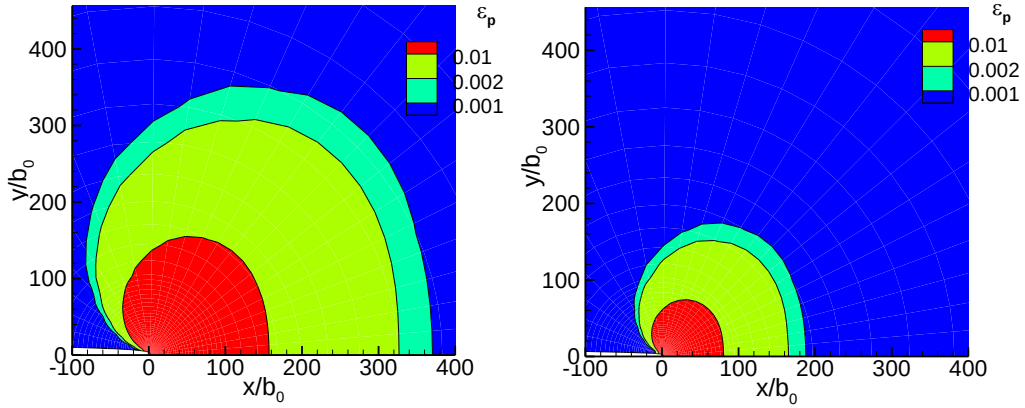

(a) (b)

Figure 6.40: Distribution of plastic strain, for plastically compressible solid, material E, $\alpha_p = 0.28$, $K_{max} = 1.0$ and $K_{min} = 0$; at the end of loading phase in 5^{th} cycle a) With overload b) Without overload

6.5.3 Near Crack Tip Fields

We now illustrate the crack tip contours of accumulated plastic strain ε_p for the 10^{th} cycle in Figs. 6.41 – 6.42 for plastically compressible solids, material B and E. Results have been generated for different ΔK and R. It has been observed that the plastic strain contours are almost similar at the end of loading and unloading phases of the 10^{th} cycle for both the materials B and E and therefore contours have been plotted here at the end of the loading phase only. From the figures, it appears that accumulated plastic strain always rise with ΔK. The influence of R is also evident, although its trend is less definite depending on material point location: closer to the tip higher R notably reduces accumulated plastic strain, whereas their sensibility to R apparently vanishes at locations far from the tip. Similar kinds of results i. e. dependence of accumulated plastic strain ε_p on ΔK and R are also observed when the materials are plastically incompressible and for brevity these results are not plotted here. In material E, when R is positive for the same ΔK, the region of intense plastic deformation, emanating from the crack surface near the symmetry plane, is more as compared to the case when R is zero. It is believed that localized deformation at the crack tip due to the dilatancy effect may have a role in it.

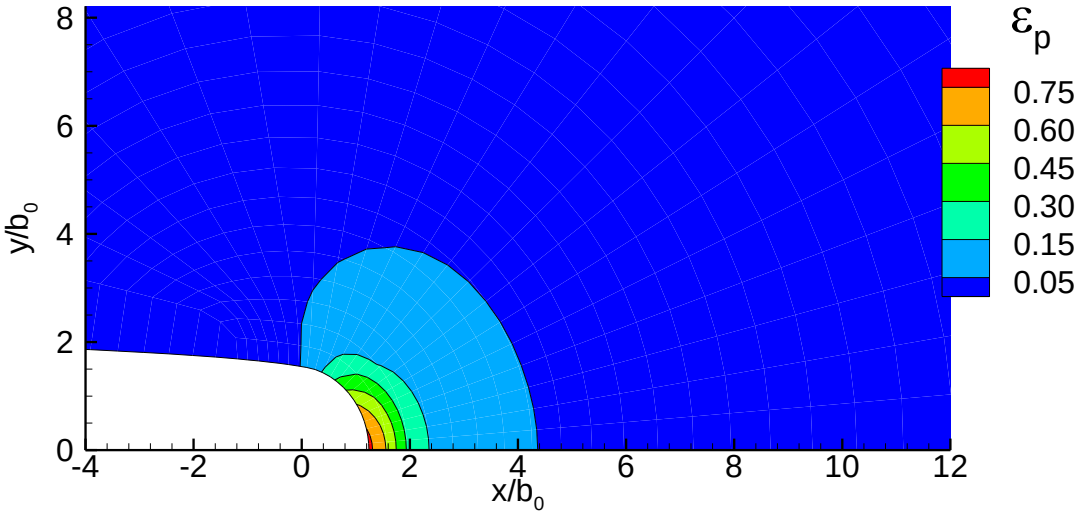
ε_p
0.75
0.60
0.45
0.30
0.15
0.05
y/b0
x/b0
0
2
4
6
8
-4
-2
0
2
4
6
8
10
12

(a)

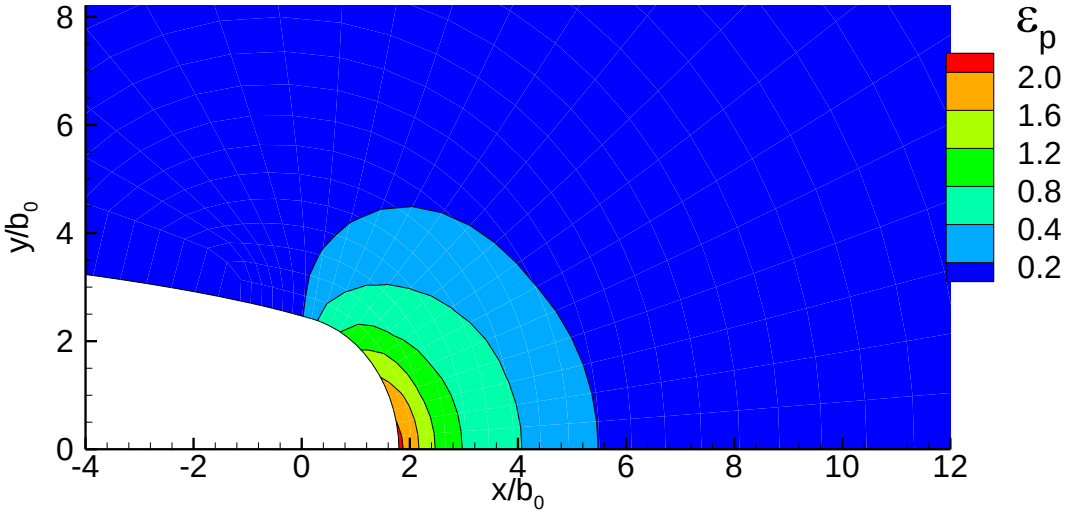
ε_p
2.0
1.6
1.2
0.8
0.4
0.2
y/b0
x/b0
0
2
4
6
8
-4
-2
0
2
4
6
8
10
12

(b)

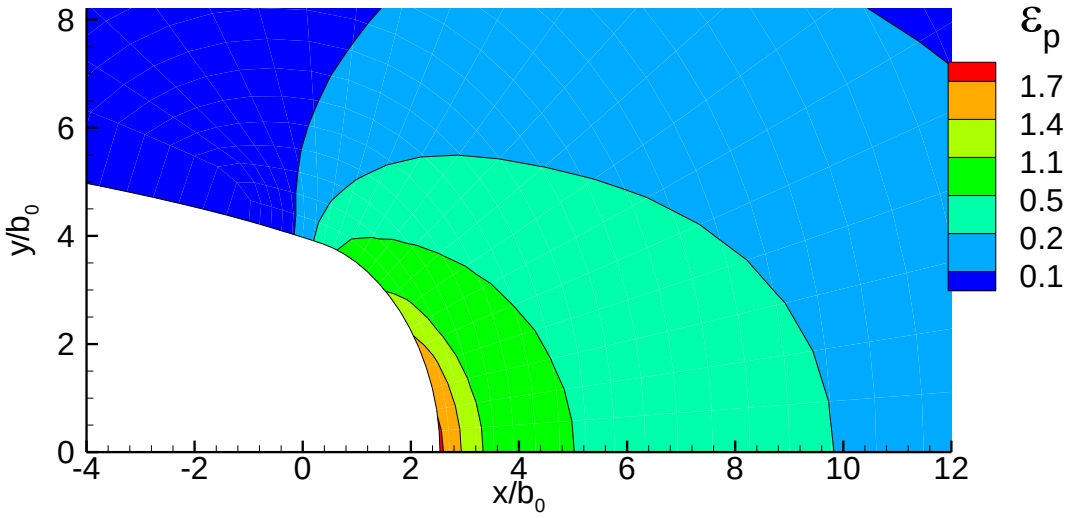

(c)

Figure 6.41: Plastic strain distribution for plastically compressible solid, material B, $\alpha_p = 0.28$, a) $K_{max} = 0.5$ and $K_{min} = 0$ b) $K_{max} = 1.0$ and $K_{min} = 0$ c) $K_{max} = 1.5$ and $K_{min} = 0.5$; at the end of loading phase for 10^{th} cycle

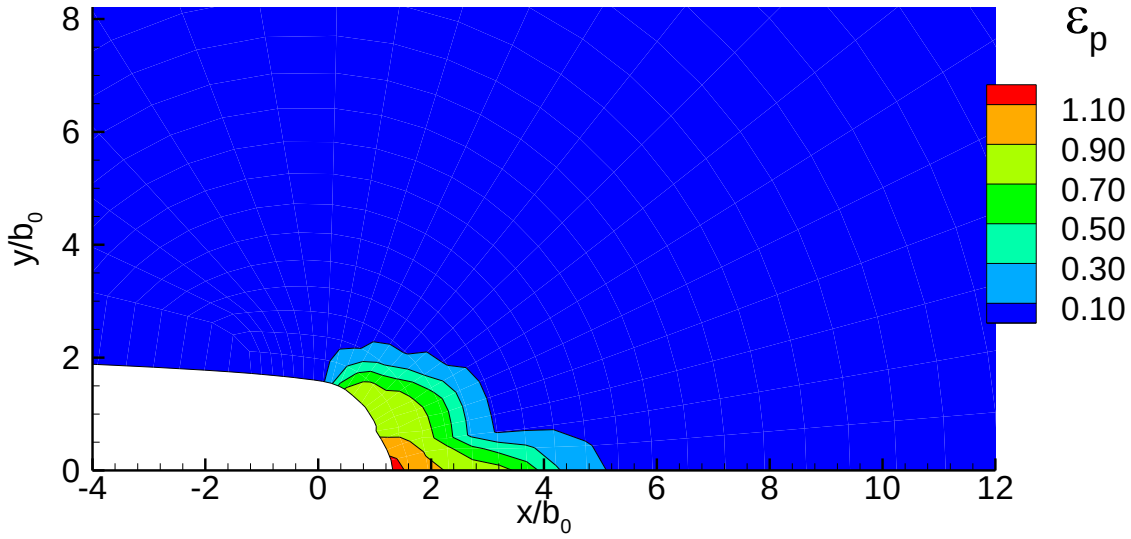

(a)

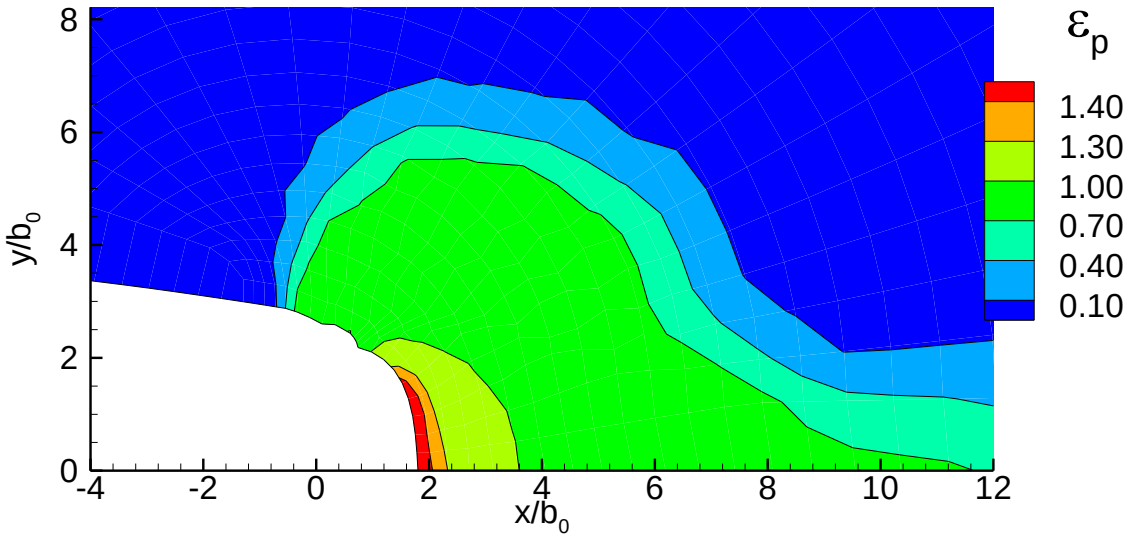

(b)

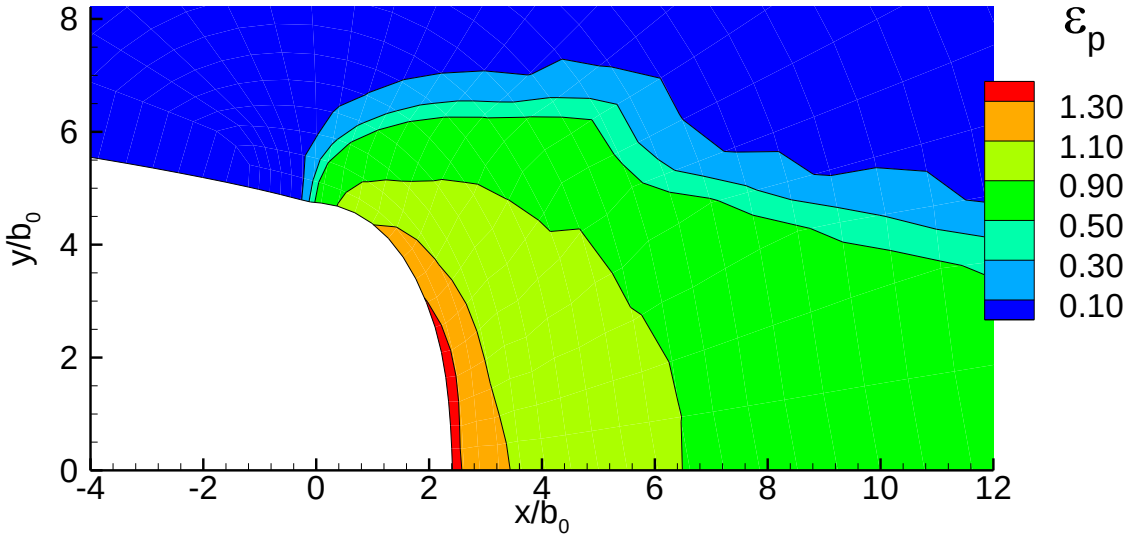

(c)

Figure 6.42: Plastic strain distribution for plastically compressible solid, material E, $\alpha_p = 0.28$, a) $K_{max} = 0.5$ and $K_{min} = 0$ b) $K_{max} = 1.0$ and $K_{min} = 0$ c) $K_{max} = 1.5$ and $K_{min} = 0.5$; at the end of loading phase for 10^{th} cycle

Although the phenomena related to shear band localization and propagation in pressure sensitive dilatant materials is not fully understood, it is believed that the hydrostatic stress plays an important role in it. Even though for monotonic loading some valuable data related to the hydrostatic stress distribution ahead of a crack tip are available for interpreation of the finite deformation fracture phenomena (Khan et al., 2017), there has been a scantiness of analogous data for cracks under cyclic loading. Figures 6.43 – 6.46 describe the hydrostatic stress distributions of plastically incompressible and compressible solids, materials B and E corresponding to $K \rightarrow K_{\max}$ and $K \rightarrow K_{\min}$. The hydrostatic stress contours are not similar during loading and unloading phase, for both the materials B and E. It is reflected from the figures that for $K \rightarrow K_{\min}$ (at the 10^{th} cycle) for materials B and E, the hydrostatic stress at the crack tip becomes negative as expected. Studies were also conducted for other loading regimes and the results were recorded at different loading cycles (other than 10^{th}); we found similar trends i.e for $K \rightarrow K_{\min}$, the hydrostatic stress at the crack tip became negative for the materials B and E. It is evident here that the peak hydrostatic stress is at the tip only at the end of loading phase for both the materials and this peak value is more in material E, however, in case of monotonic loading this peak hydrostatic stress occurs at some distance ahead of the crack tip. The residual compressive stress due to the effect of fatigue loading may be the reason behind this. When there is plastic compressibility the magnitude of these hydrostatic tension peaks gets smaller.

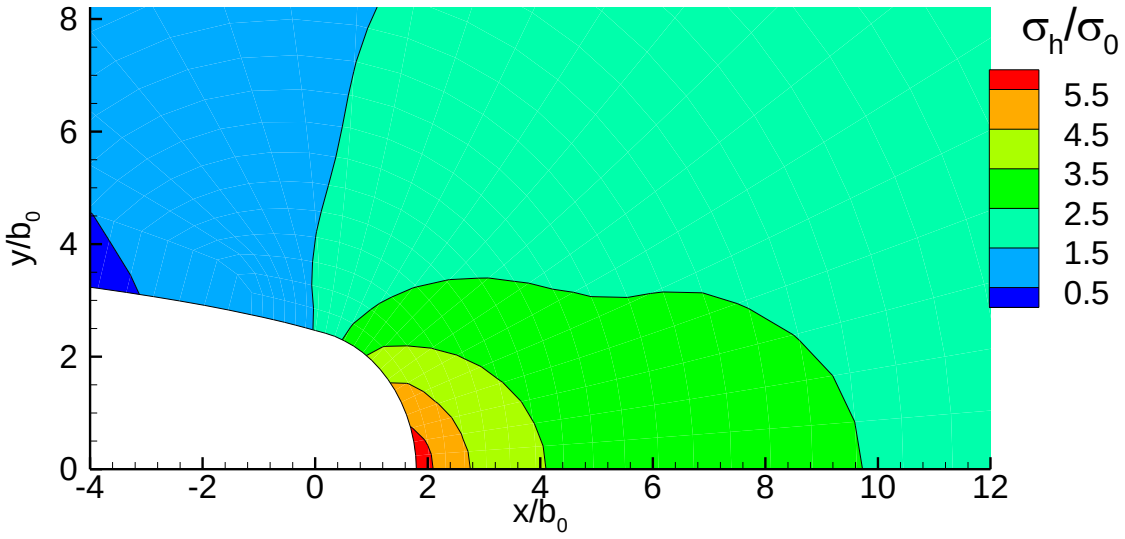

(a)

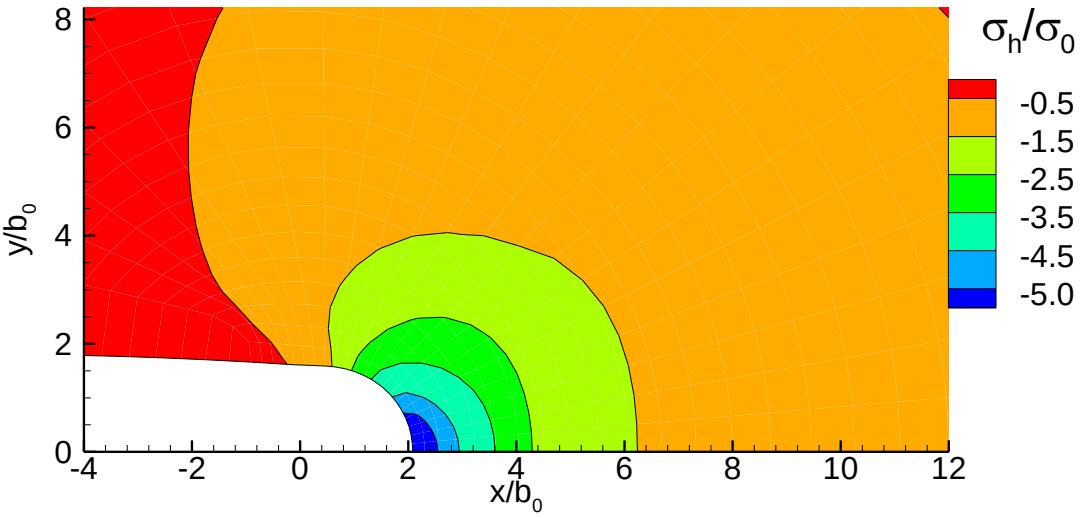

(b)

Figure 6.43: Hydrostatic stress for plastically incompressible solid, material B, $K_{max} = 1.0$ and $K_{min} = 0$; a) At the end of loading phase b) At the end of unloading phase for 10^{th} cycle

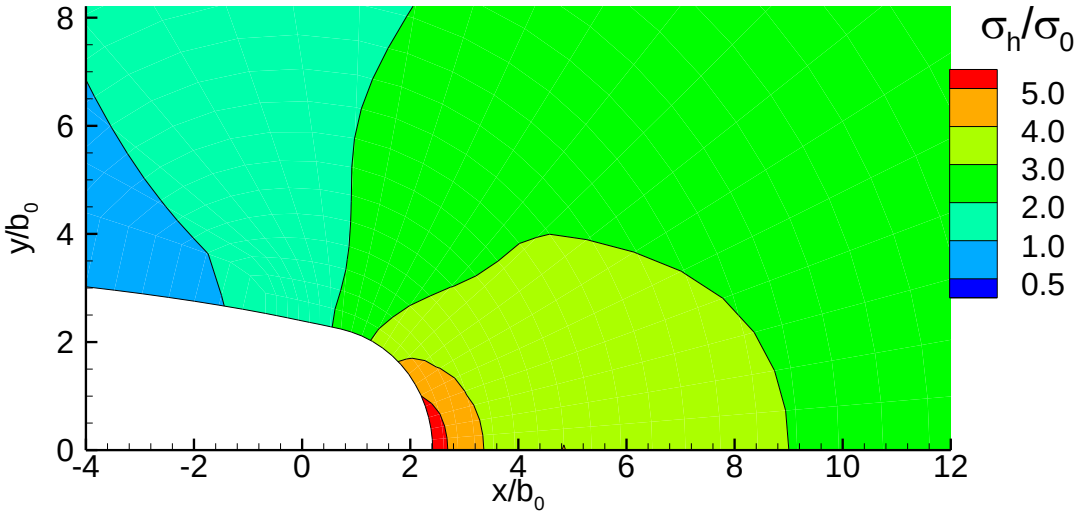

(a)

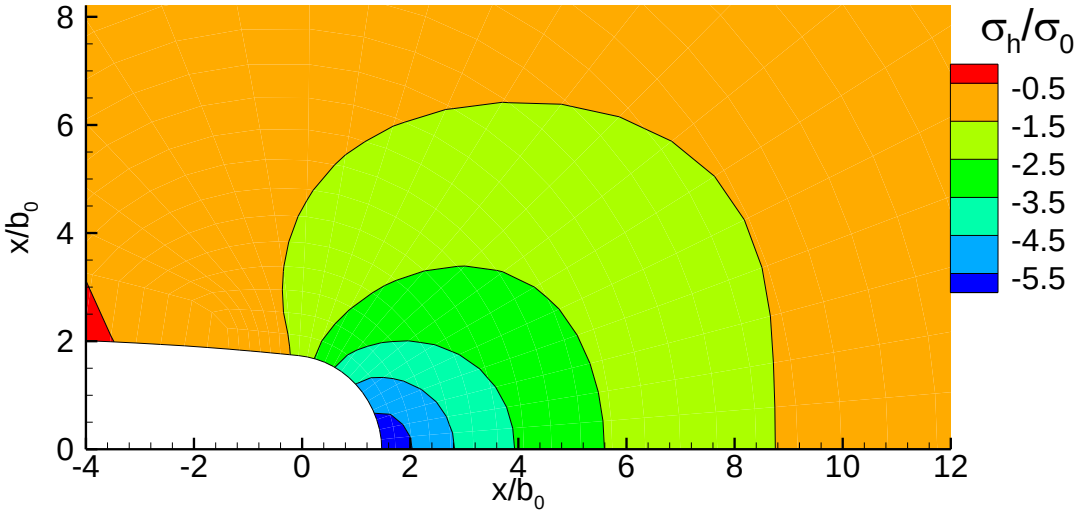

(b)

Figure 6.44: Hydrostatic stress for plastically compressible solid, $\alpha_p = 0.28$, material B, $K_{max} = 1.0$ and $K_{min} = 0$; a) At the end of loading phase b) At the end of unloading phase for 10^{th} cycle

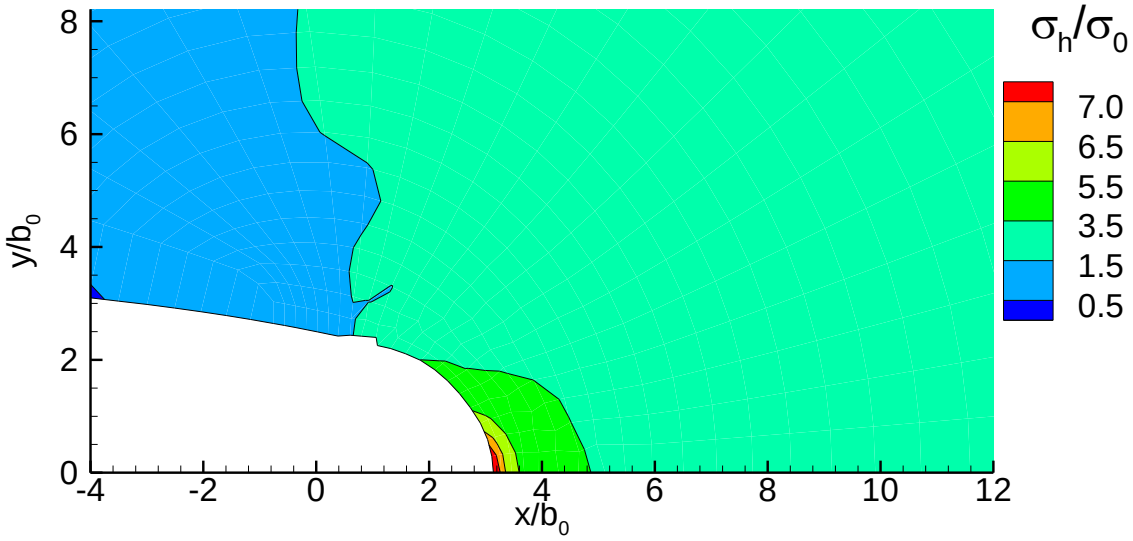

(a)

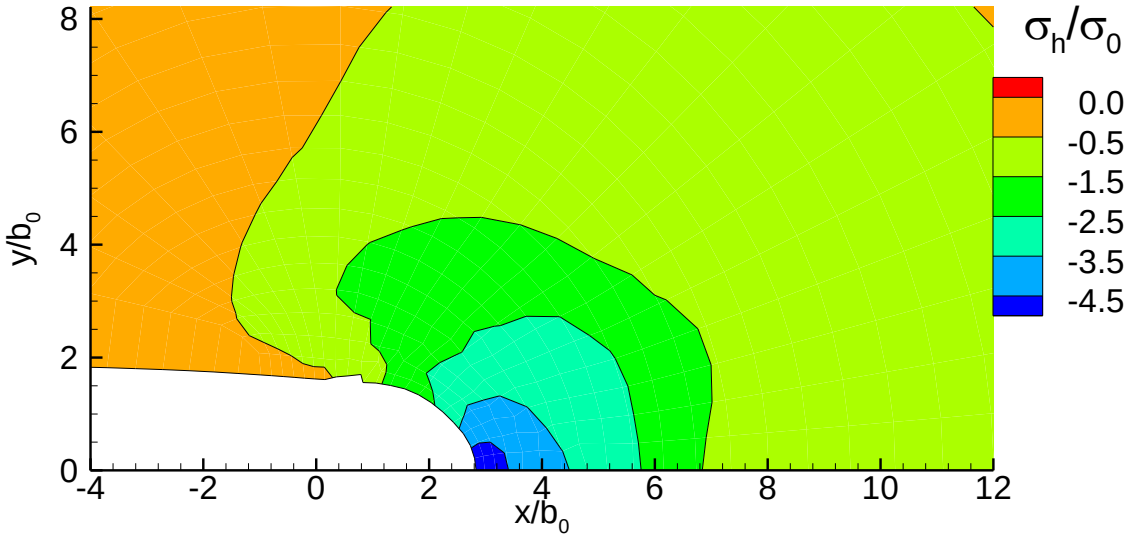

(b)

Figure 6.45: Hydrostatic stress for plastically incompressible solid, material E, $K_{max} = 1.0$ and $K_{min} = 0$; a) At the end of loading phase b) At the end of unloading phase for 10^{th} cycle

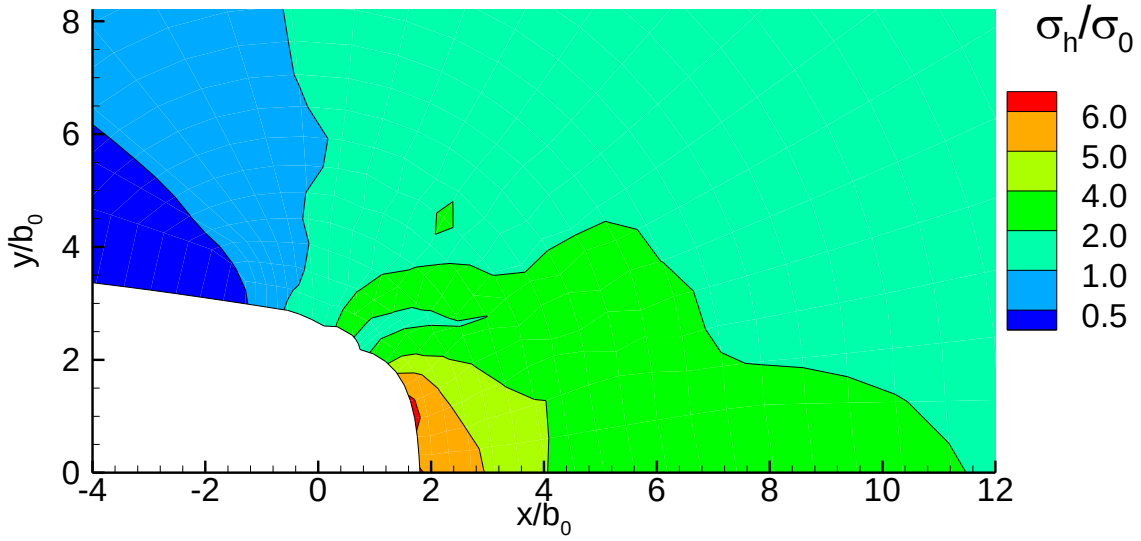

(a)

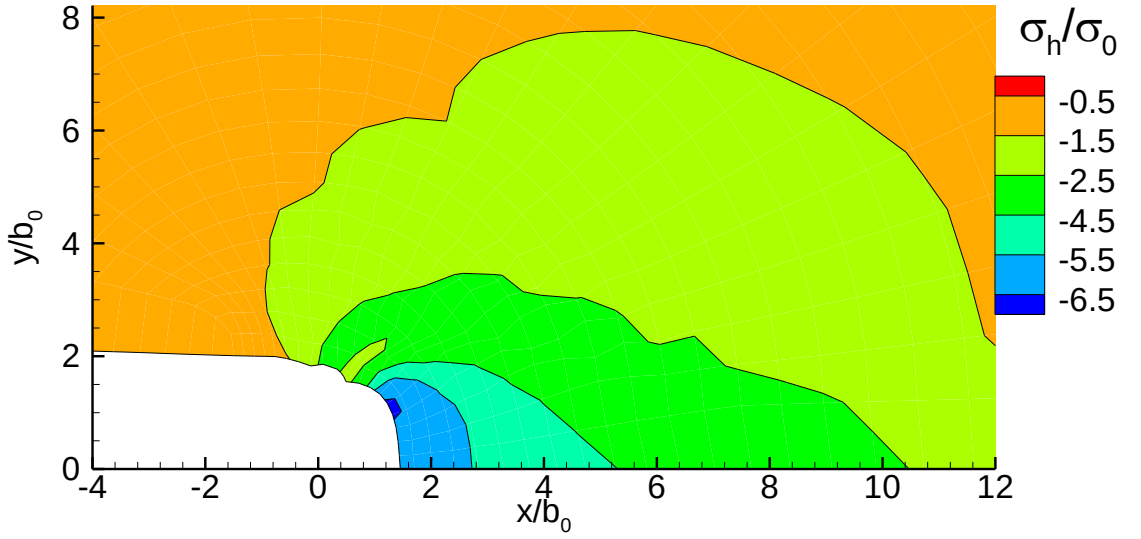

(b)

Figure 6.46: Hydrostatic stress for plastically compressible solid, $\alpha_p = 0.28$, material E, $K_{max} = 1.0$ and $K_{min} = 0$; a) At the end of loading phase b) At the end of unloading phase for 10^{th} cycle

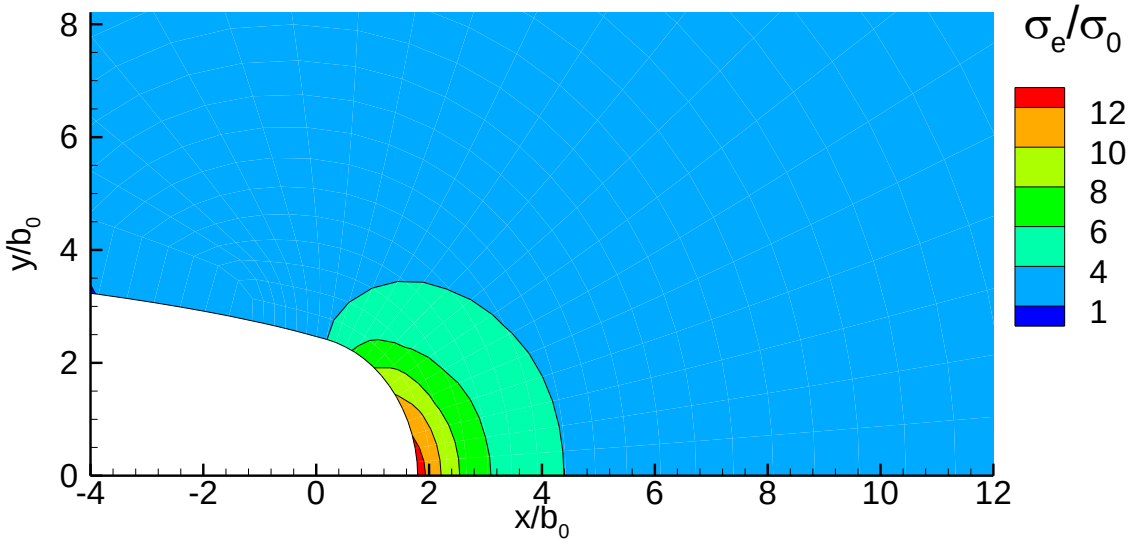

(a)

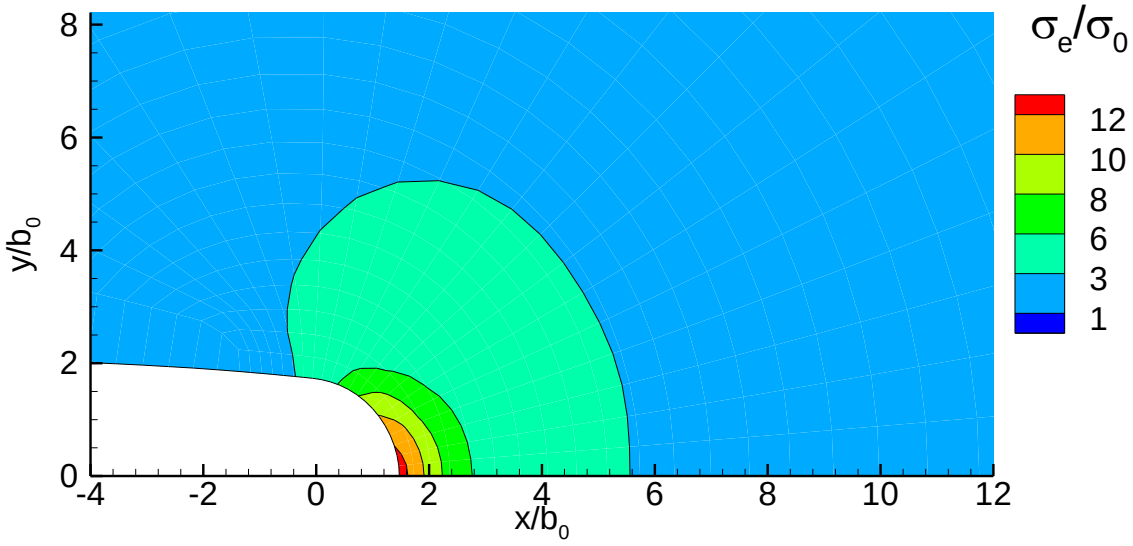

(b)

Figure 6.47: Distributions of normalized effective stress measures for plastically compressible solid, $\alpha_p = 0.28$, material B, $K_{max} = 1.0$ and $K_{min} = 0$; a) At the end of loading phase b) At the end of unloading phase for 10^{th} cycle

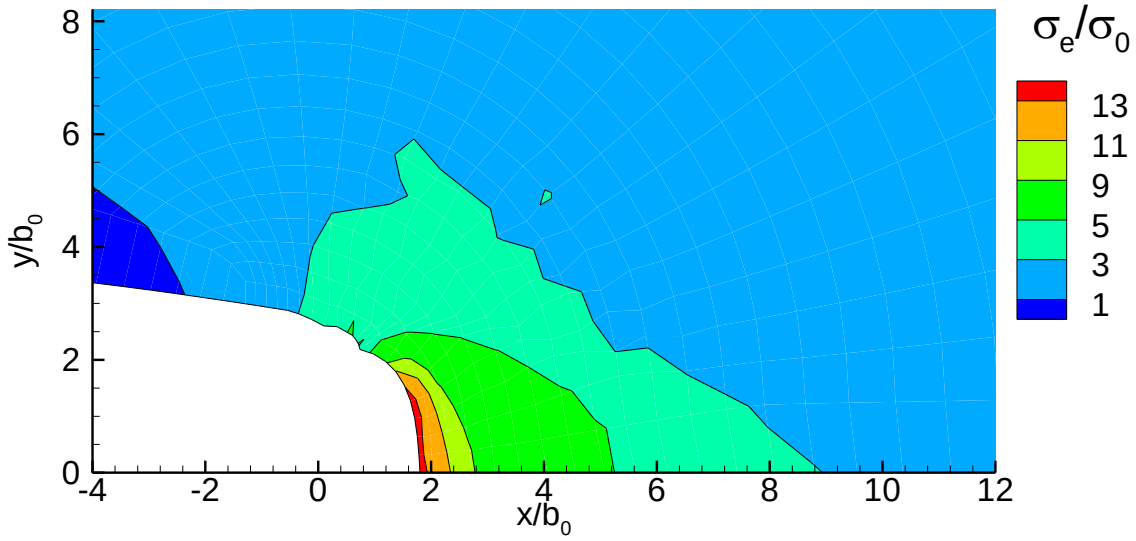

(a)

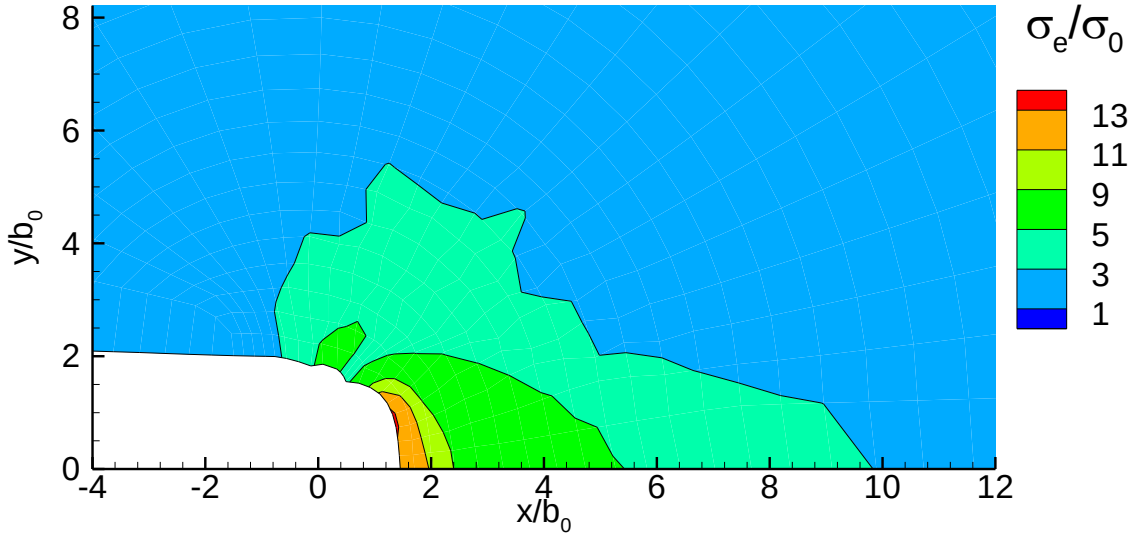

(b)

Figure 6.48: Distributions of normalized effective stress measures for plastically compressible solid, $\alpha_p = 0.28$, material E, $K_{max} = 1.0$ and $K_{min} = 0$; a) At the end of loading phase b) At the end of unloading phase for 10^{th} cycle

Next, distributions of the work conjugate effective stress, σ_e are shown for plastically compressible solids, material B and E, in Figs. 6.47 – 6.48 for the same 10^{th} cycle. Like monotonic loading, it is reflected that the band of increased σ_e overlaps the band of increased straining. At the end of loading and unloading there is almost no change in the distributions of the effective stress measures and peak value of the effective stress is more in material E. Like the peak hydrostatic tension, the peak effective stress value occurs at the tip only which is in contrast to the distribution of monotonic loading.

6.6 Some Results under Monotonic Loading (Plastic Non-normality Condition)

Subsequent study concerns to the role of plastic non-normality on the crack tip deformation as well as near tip field quantities and for the sake of brevity these effects are restricted to monotonic loading case only. As the code is ready, further numerical investigation may also be easily carried out to examine their influence on the solution based on cyclic loading. The following results have been generated when the geometry is subjected to monotonic loading only.

6.6.1 Crack Tip Deformation

Here, some results are provided for non-normality condition just to compare the effect with normality condition. For material E where the variation of flow strength is hardening-softening-hardening type and the flow rule of non-normality kind, slightly abrupt jumps take place in the curve, Fig. 6.49c. In Fig. 6.49b similar plots are there for material E where the constitutive equation is said to follow plastic normality rule and in this case it is visible that considerable amount of abrupt jumps take places in the curve. It is believed that localized deformation at the crack tip due to the presence of softening and compressibility may have a

role in this jump/flutter. In the literature it is well established that non-normality appears as a result of dilatancy effect and therefore when we model material E with non-associative flow rule it may represent more realistic behavior, Figs. 6.46b and 6.46c. In the present study the fluttering is reduced to a significant extent when material E is modeled using non-normality flow rule.

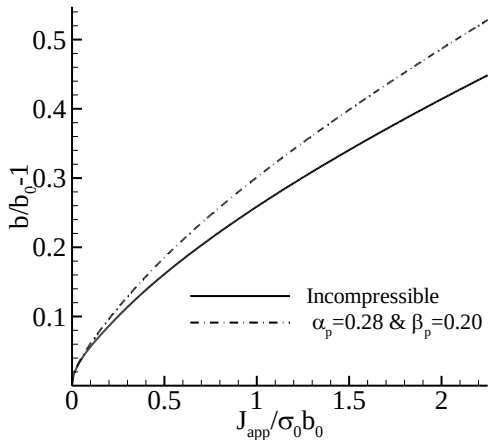

(a)

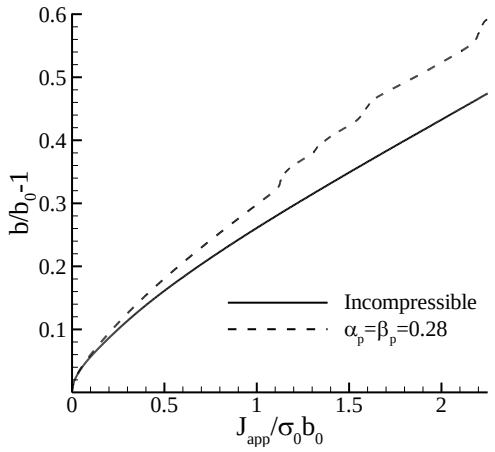

(b)

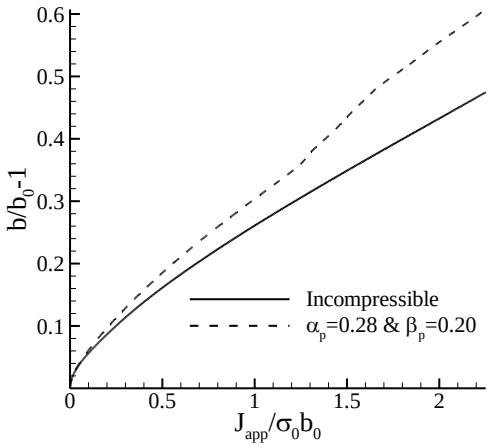

(c)

Figure 6.49: Crack-tip opening displacement $\delta_t(= b/b_0 - 1)$ versus applied *J*-integral, J_{app} , $J_{app}/(\sigma_0 b_0)$ = 2.25 a) Material B, b) Material E, plastically incompressible and compressible conditions ($\alpha_p = \beta_p = 0.28$), c) Material E, plastically incompressible and compressible conditions (α_p =0.28 & β_p =0.20)

6.6.2 Near Crack Tip Fields

We now illustrate the crack tip blunting and the contours of accumulated plastic strain ε_p for materials B and E in Figs. 6.50 - 6.51, respectively. It is mentioned here that for the largest value of the J_{app}considered in the present calculations, rehardening of material E takes place i. e. the value of ε_p generated is 0.7 which is greater than ε_2 whose value is 0.6. It is observed from the figures that when the materials are plastically incompressible, maximum plastic strain concentration occurs on the surface of the crack and extends along the crack blunting crack surface. The nature of the crack tip blunting is different in materials B and material E. Region of the highest plastic strain is more in material E and less in material B. On the other

hand, when the material is plastically compressible, there is evolution of region of localized deformation in front of the initial crack tip in material E but not in material B. In materials E, there is a region of intense plastic deformation emanating from the crack surface near the symmetry plane and this region extends in the positive x direction. This localized deformation in turn affects the shape of the blunted crack tip and it is visible in Fig 6.48b. From this figure, it may be commented that the softening (or softening-hardening) has a major role in crack tip blunting. For material B where the hardness function is of hardening-hardening type, the localized deformation is not visible. For material B, the use of normality and non-normality flow rules does not make any difference; however, there is significant amount of difference in the regions of intense plastic deformation at the crack tip in the material E. In case of non-normality flow rule the size of the region of intense plastic deformation at tip is noticeably small than that of the normality condition. In the non-normality case, the direction of plastic straining being not perpendicular to the yield surface might have reduced the evolution of the localized intense plastic deformation region.

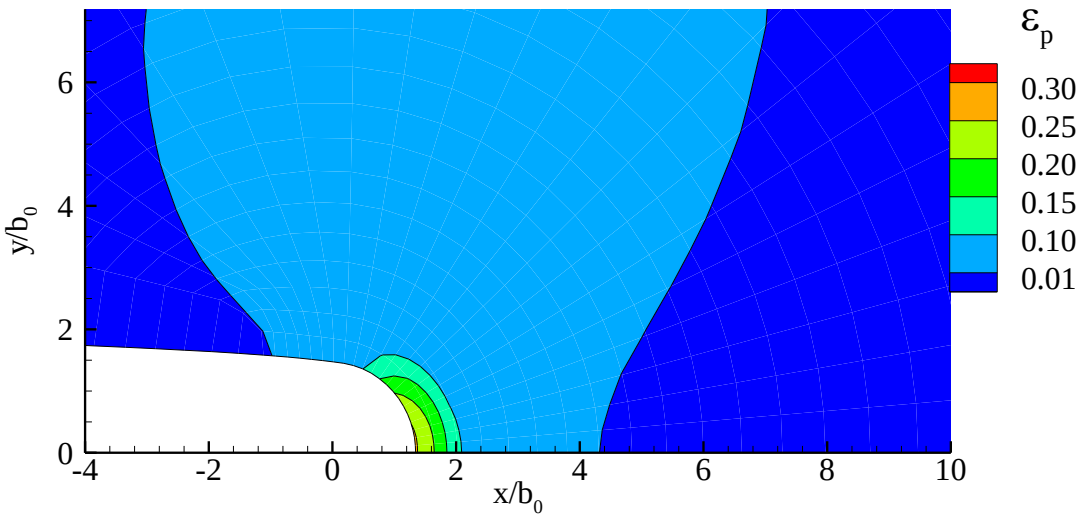

(a)

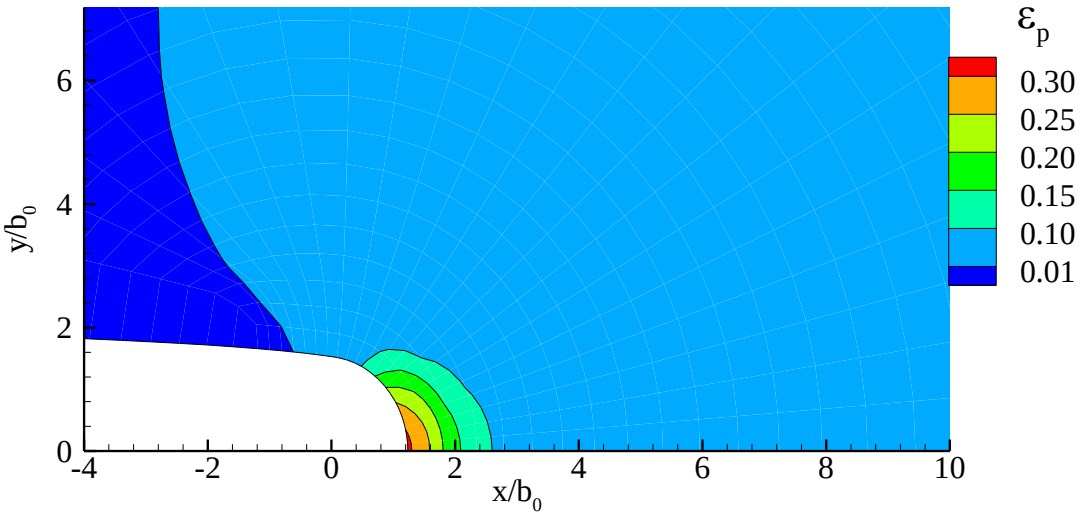

(b)

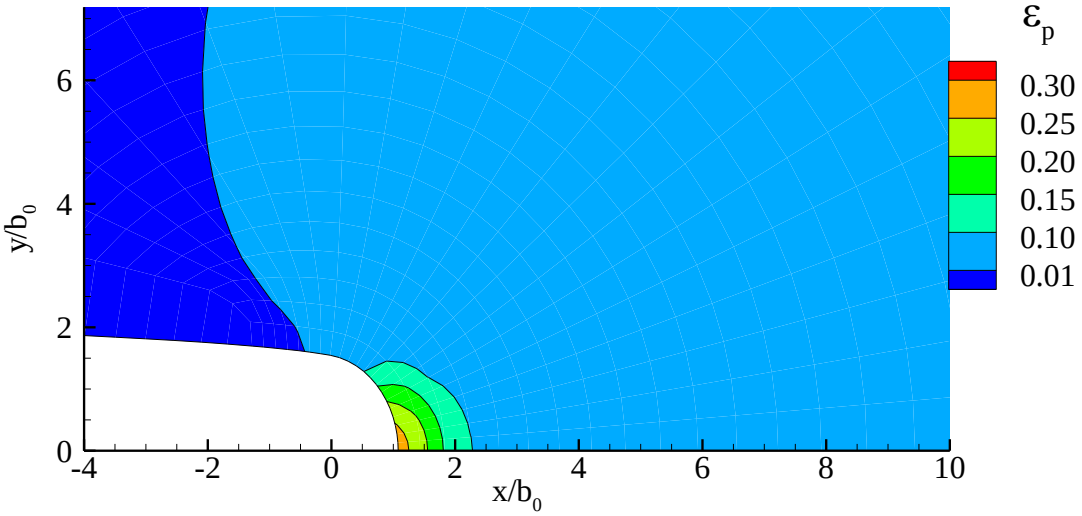

(c)

Figure 6.50: Distribution of accumulated plastic strain ε_p at the crack tip of maerial B, $J_{app}/(\sigma_0 b_0)$ = 2.25. a) Plastically incompressible, b) Plastically compressible ($\alpha_p = \beta_p =$ 0.28), c) plastically compressible (α_p =0.28 & β_p =0.20)

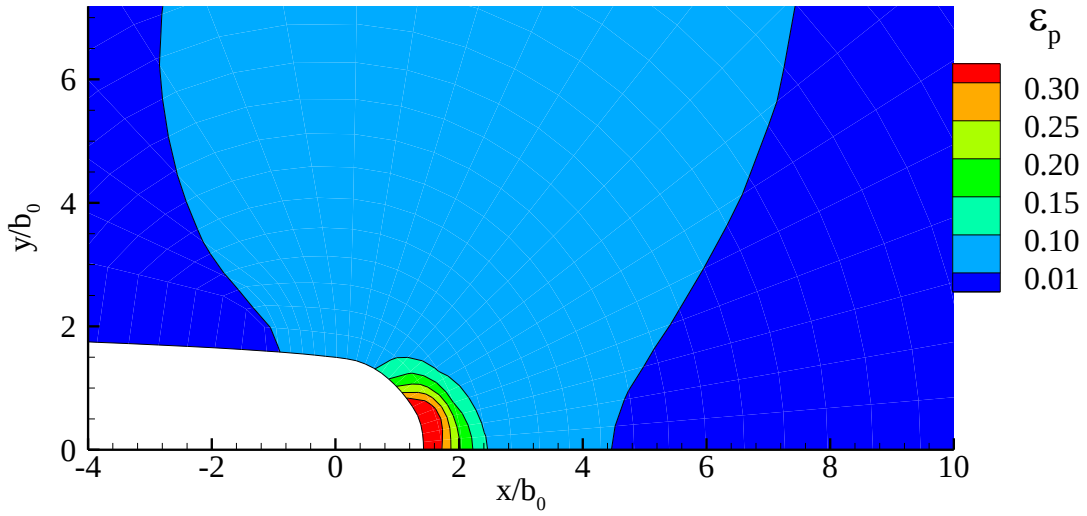
ε_p
0.30
0.25
0.20
0.15
0.10
0.01
y/b_0
x/b_0
0
2
4
6
-4
-2
0
2
4
6
8
10

(a)

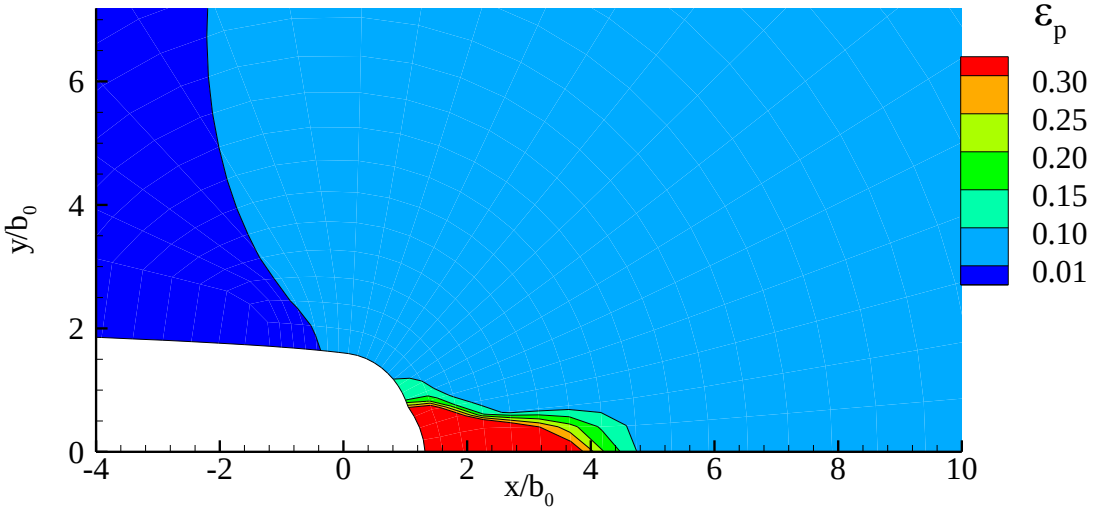
ε_p
0.30
0.25
0.20
0.15
0.10
0.01
y/b_0
x/b_0
0
2
4
6
-4
-2
0
2
4
6
8
10

(b)

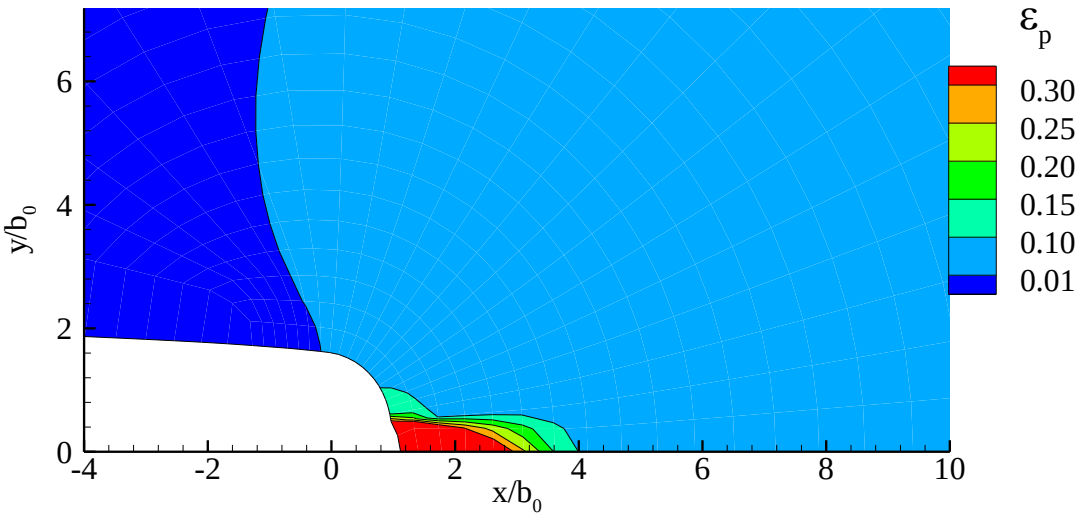

(c)

Figure 6.51: Distribution of accumulated plastic strain ε_p at the crack tip of maerial E, $J_{app}/(\sigma_0 b_0)$ = 2.25. a) Plastically incompressible, b) Plastically compressible ($\alpha_p = \beta_p =$ 0.28), c) plastically compressible (α_p =0.28 & β_p =0.20)

For the classical solution with the Huber-Mises-Hencky yield criterion, the volume change is caused only by elastic deformations while for pure shear deformation it is equal to zero. For the plastically dilatant materials, however, the volume change can be observed during plastic deformation. In order to explain the role of plastic non-normality in near crack tip volume change, Fig. 6.52 illustrates the distribution of ε_{vol} for material E, where $\varepsilon_{vol} = \int_0^t \mathrm{tr}(\boldsymbol{d})\mathrm{d}t$. It should be mentioned here that as ε_{vol} is defined in terms of total rate of deformation tensor $(\boldsymbol{d})$ it includes a small elastic contribution from $\boldsymbol{d}^e$. From the distributions it is clearly visible that the volumetric strain is to some extent more in front of the crack tip for plastically normality conditions as compared to that of plastically non-normality condition.

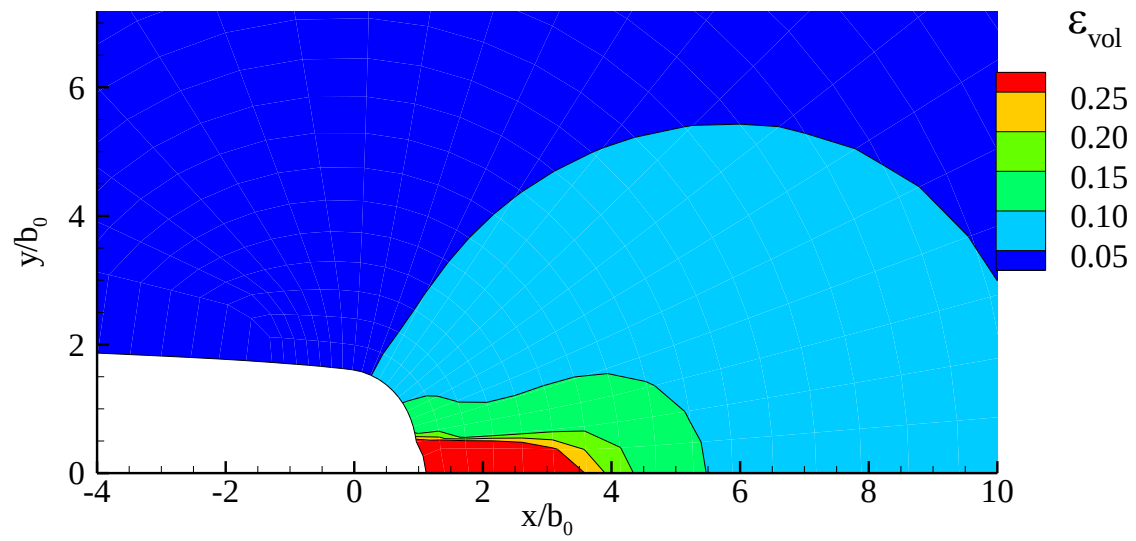

(a)

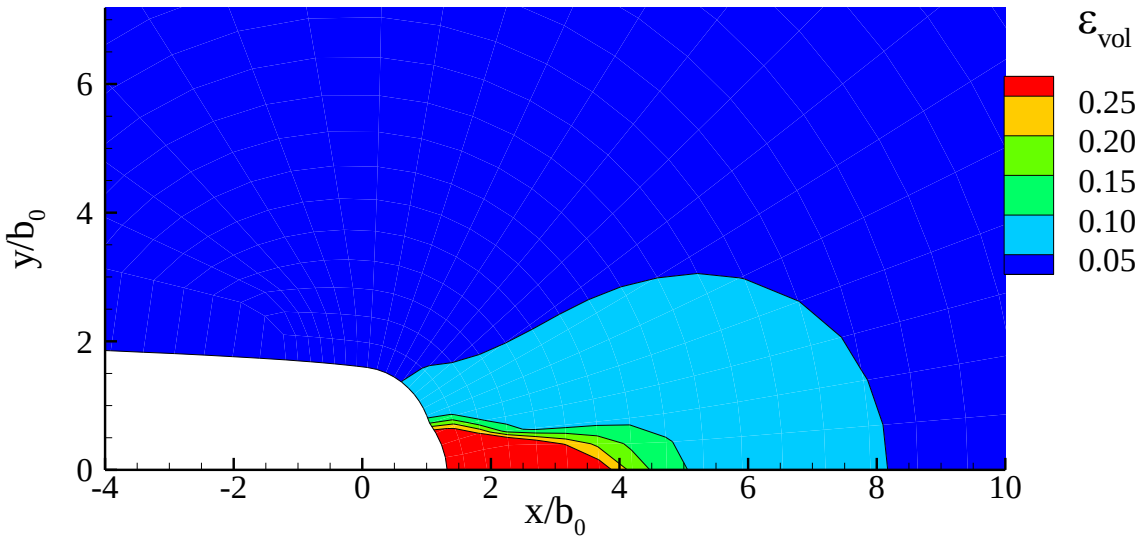

(b)

Figure 6.52: Distribution of volumetric strain ε_{vol} at the crack tip, $J_{app}/(\sigma_0 b_0)$ = 2.25. material E a) $\alpha_p = 0.28$ & $\beta_p = 0.20$ b) $\alpha_p = \beta_p = 0.28$

The dilational deformation comes from pressure-sensitive yielding and non-normality flow rule. Therefore, it seems to be relevant to study the distribution of the hydrostatic stress in the crack tip region and how it is influenced by the plastic deformation for the elastic-viscoplastic materials. The hydrostatic stress distribution has been investigated here considering constant elastic stiffness. Figs 6.53 describes the hydrostatic stress distributions of the material E for plastically incompressible as well as compressible states considering both associative and non-associative flow rules. It should be again mentioned here that at the load level of $J_{\text{app}}/(\sigma_0 b_0)$ = 2.25, material E is in the region of rehardening. At other load levels also we carried out the computations and from this it can be mentioned that the location of the peak hydrostatic stress is changed with respect to the crack tip when the applied load is varied. The distribution of hydrostatic stress is very much qualitatively different for plastically incompressible and compressible conditions. Again when the constitutive equation is framed using non-normality flow rule the hydrostatic stress distribution/ localization is reasonably unusual than that of the normality flow rule. There are two regions along the symmetry plane where there are local peaks; in normality conditions these two local peaks in σ_{h} are at x/b_0 = 3 and at x/b_0 = 5 whereas for the non-normality conditions one local peak at the crack tip and the other peak (with slightly lesser stress intensity) at x/b_0 = 4.2. When there is plastic compressibility the magnitude of these hydrostatic tension peaks gets smaller. When we use normality flow rule it is apparent that there is significant amount of stress reduction on the crack tip surface but it is not same while using non-normality flow rule though the reduction in the magnitude of the hydrostatic tension peak is common because of the softening. Therefore, it may be concluded here that

the combination of plastic compressibility, hardening slope, flow rule and applied load has a strong effect in the near crack tip hydrostatic stress distribution.

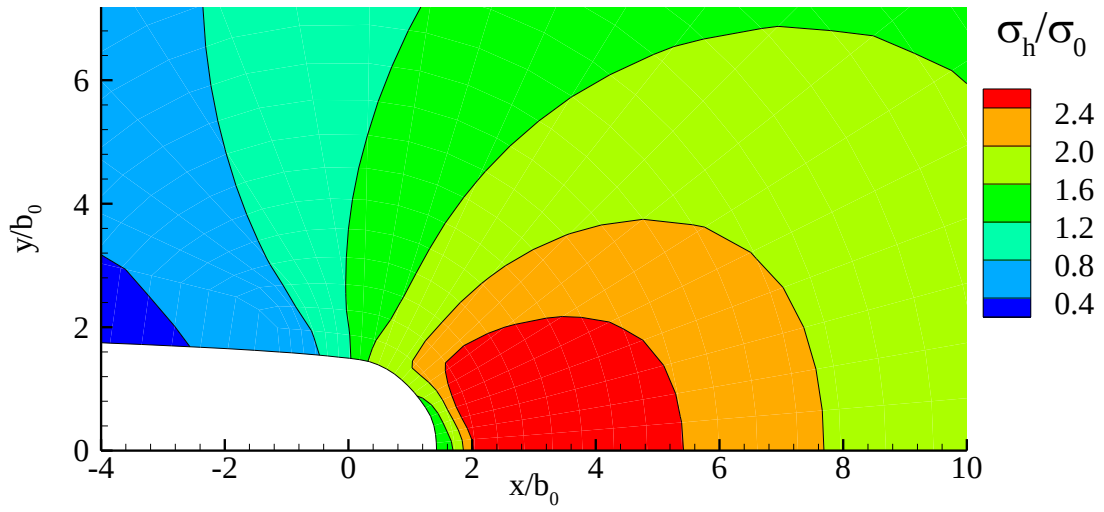

(a)

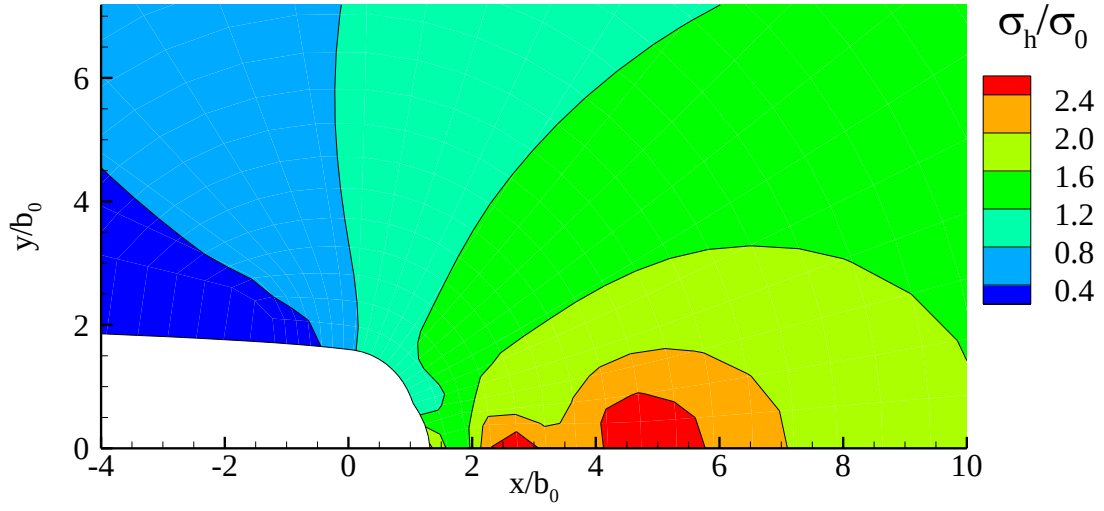

(b)

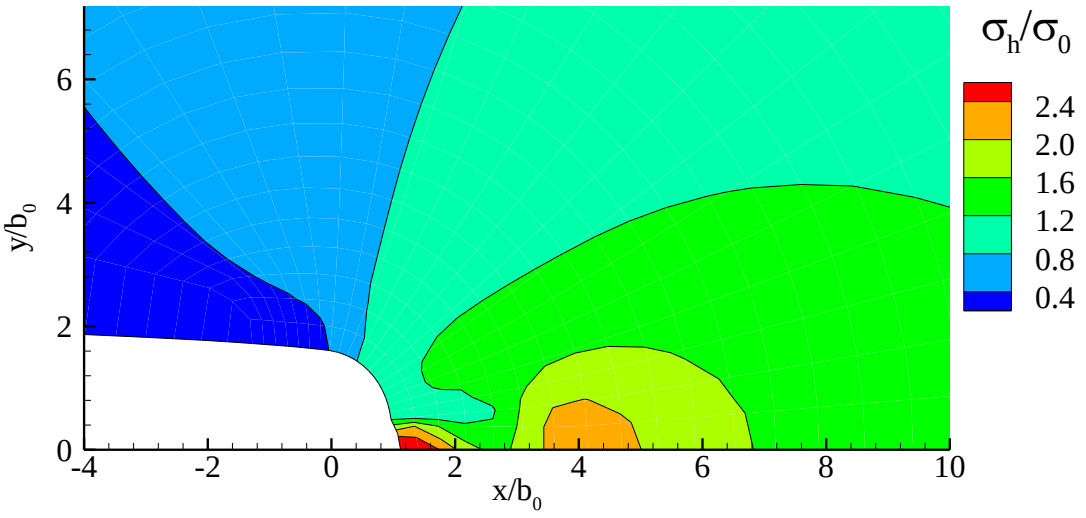

(c)

Figure 6.53: Normalized hydrostatic stress distribution at the crack tip vicinity for material E, $J_{app}/(\sigma_0 b_0)$ = 2.25. a) Plastically incompressible, b) Plastically compressible ($\alpha_p = \beta_p =$ 0.28), c) Plastically compressible ($\alpha_p = 0.28$ & β_p =0.20)

Next we illustrate the distributions of the work conjugate effective stress, σ_e for material E while using the plastic non-normality flow rule in Figs. 6.54. Here, at $J_{app}/(\sigma_0 b_0)$ = 2.25 like the hydrostatic stress distributions, for normality condition, there are two regions of increased stress measures; one peak is at $x/b_0 = 3$ and the other is at $x/b_0 \approx 5$ due to the dependence of equivalent stress on the hydrostatic stress whereas for non-normality one peak of work conjugate effective stress measures at the crack tip and the other peak is at $x/b_0 = 3.6$. So, compairing the distribution of the effective stress measures one can clearly make out the difference of using normality and non-normality flow rule.

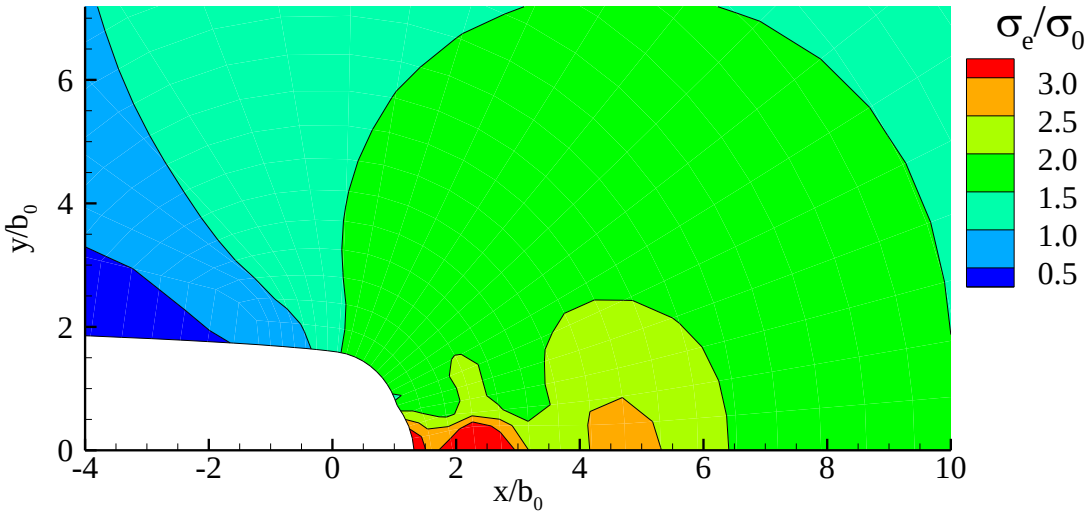

(a)

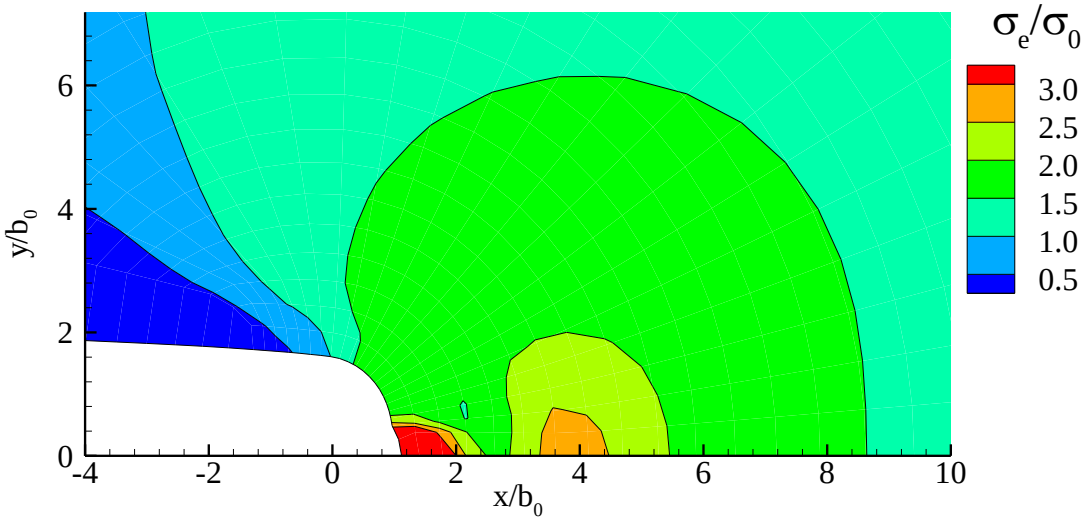

(b)

Figure 6.54: Effective stress distribution at the crack tip vicinity for material E, $J_{app}/(\sigma_0 b_0) = 2.25$. a) Plastically compressible ($\alpha_p = \beta_p = 0.28$), b) Plastically compressible ($\alpha_p = 0.28$ & $\beta_p = 0.20$)

6.7 Concluding Remarks

In this chapter, the behavior of the constitutive equations, for plastically compressible rate dependent elastic viscoplastic solids with hardening-hardening and hardening-softening-hardening flow rules described in chapter 5, has been investigated under monotonic and cyclic loadings for a mode I crack. Role of both plastic normality as well as plastic non-normality has been explored. Various aspects of the combination of plastic compressibility and softening or softening-hardening material response have been studied in detail. A number of interesting observations emerged from the present finite element calculations of crack tip deformations and fields.